scientific reports

Check for updates

OPEN

Prediction and assessment of optimal concrete compositions for overall radiation protection and reduced global warming potential

Sanchit Saxena[1] & Hrishikesh Sharma[2]✉

Developing an efficient radiation-shielding concrete composition holds paramount importance for nuclear, medical, and defence facilities. The intricate interactions between various radiation particles and materials across different energy ranges present challenges in designing effective and resilient overall shielding structures. This study presents a novel approach that integrates machine learning and genetic algorithms (GA) to optimize concrete compositions for enhanced radiation shielding against gamma and neutron rays across a wide energy spectrum. By leveraging these advanced techniques, six compositions (concrete_1—concrete_6) spanning different density ranges were derived from an extensive database developed from the previous experimental researches. Subsequently, the shielding effectiveness of these compositions against all radiation particles was evaluated and compared using the OpenMC Code. The findings revealed that the proposed concrete_5 and concrete_6 compositions, comprising iron, boron, nickel, and tungsten at specified weight fractions, outperform other state-of-the-art compositions in overall radiation shielding. Furthermore, the analysis indicated a 65.89% reduction in Global Warming Potential (GWP) with the adoption of concrete_6 composition compared to conventional concrete composition.

Keywords Radiation attenuating concrete, Monte-Carlo simulation, Multi-objective constrained genetic algorithm, Machine learning, Sustainability

Nuclear energy has long been acknowledged as a crucial component of the global energy balance, providing a sustainable, dependable, low-carbon electricity source[1]. The growing concerns regarding climate change and the urgent necessity for transitioning to sustainable energy sources have led to a substantial increase in the significance of nuclear power and its infrastructure, notably nuclear power plants (NPPs)[2]. However, NPPs are often connected to the fear of disastrous accidents such as the Chernobyl disaster, Soviet Union (1986)[3]and Fukushima disaster, Japan (2011)[4]. Radiation plays a critical role in nuclear disasters, exerting immediate and long-term impacts extending over vast areas and affecting a wide range of flora and fauna[5,6]. The influence of radiation can extend for thousands of kilometers, with profound consequences on ecosystems[7]. To ensure the sustained success and public acceptance of nuclear energy and radiation-related risks, there is a requirement to provide safety to humans and animals from radiation exposure risks.

The three fundamental principles used to minimize the risk of radiation exposure are time of exposure, distance, and shielding[8]. With over 1 million people living within 75 km of 152 NPPs around the globe[9], a large area of the ecosystem and population will be at risk during any possible accident or radiation threat. In such a scenario, there will be many constraints in decreasing the exposure time or increasing the distance, thereby having a minimal effect on mitigating the radiation effects. Shielding is the most effective principle to mitigate any such accident, as it can potentially confine radiation within its bounds. In Chernobyl (1986), the casket around Reactor 4 contained radiation, reducing exposure to emergency responders[3]. Similarly, at Fukushima (2011), concrete walls and water barriers helped prevent the spread of radioactive materials[5]. These incidents highlight the vital role of shielding in protecting both people and the environment from radiation in nuclear disasters.

Concrete is used as a conventional construction and shielding material in NPPs and other radiation shielding structures due to its strength in withstanding tough conditions, good shielding properties against gamma rays

[1]Research Scholar, Department of Civil Engineering at IIT Guwahati, Guwahati, Assam, India781039. [2]Associate Professor, Department of Civil Engineering, Indian Institute of Technology (IIT) Guwahati, Guwahati 781039, Assam, India. ✉email: shrishi@iitg.ac.in

and neutrons—attributed to its mixture of light and heavy nuclides—and its cost-effectiveness compared to other efficient shielding materials[10–13]. Various investigations have been done on improving the gamma and neutron radiation attenuation capacity of concrete by varying the types of aggregates[14–34], improvising cementitious materials[35–45], developing high-performing concrete (HPC)[13,33,46–48], and by adding other additional materials in concrete[49–68]. Low-carbon radiation shielding materials have also gained significant attention due to their ability to address both environmental sustainability and radiation protection requirements. Recent studies have explored the incorporation of industrial byproducts and wastes like steel slag, fly ash, and waste powders such as marble and granite, and recycling of cathode ray tubes, which enhance the shielding performance while reducing its carbon footprint[30,31,38,69–73]. Various materials used in the researches are shown in Fig. 1. The shielding capacity of these material compositions against discrete energies of gamma radiations was tested using experimental set-ups containing a gamma radiation source, scintillator, and a detector. Simulations were performed using various Monte-Carlo codes i.e., FLUKA[32,39,44,62,64], MCNP6[15,27,54,59,61,63], Geant4[53], and NXcom[21,39,44,53,54,59,63,65], to evaluate the shielding properties of different compositions of concrete against neutron and gamma radiation.

Inside an NPP, a nuclear fission reaction produces fission fragments accompanied by gamma rays and neutrons[74]. Therefore, the shielding material developed for an NPP should be strong enough to withstand accidental loadings and showcase high shielding efficiency against gamma and neutron rays. In addition to radiation shielding, mechanical strength is critical for ensuring efficient protection. However, selecting the optimal composition of elements/ materials for the design is essential before addressing mechanical strength. Notably, this is challenging because high-density materials/elements (for example—lead, concrete) showcase better attenuation against gamma rays, whereas low-density materials/ elements (for example – heavy water, boron, polyethylene) show better shielding against neutron rays[75,76]. Moreover, different elements show different attenuation values in different energy ranges[77]. In the literature, despite numerous configurations and materials

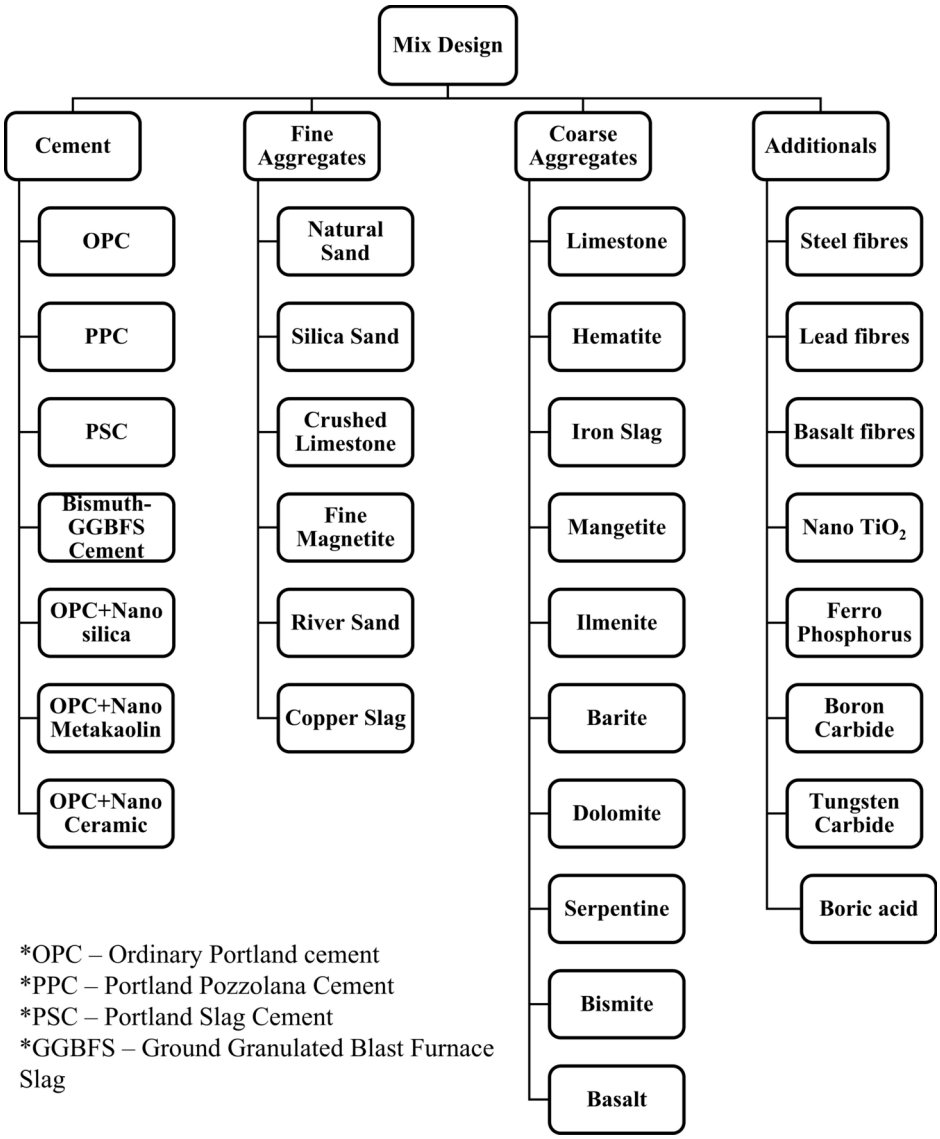


Fig. 1. Materials for radiation shielding concrete.

being used to improve conventional concrete's gamma and neutron attenuation properties, the best composition/combination of materials that offer the best radiation attenuation properties against neutron and gamma rays over a wide range of energy has not been discussed.

To address these challenges, this study introduces novel concrete compositions that exhibit the highest level of shielding performance against gamma and neutron rays over the entire energy spectrum of nuclear fission reactions. The proposed compositions represent a substantial leap forward compared to existing state-of-the-art materials, as they effectively address the complex and contrasting behaviour of different matter-particle interactions while maintaining the required balance. By considering wide energy ranges and comprehensively analyzing particle behaviour, the study successfully accounts for the unpredictability of potential radiation-related incidents or accidents in real-life scenarios. This ensures the practical applicability of the developed compositions and guarantees superior shielding performance in developing radiation-protected structures and highly resilient NPP structures. Additionally, this work examines the environmental implications of the proposed compositions, quantifying their impact on sustainability. The results reinforce the composition's eco-friendliness, making them suitable for developing highly resilient NPPs and other radiation shielding structures and contributing to long-term sustainability. The workflow, as shown in Fig. 2, has been followed to achieve the required objective.

Methodology

The methodology employed in this study comprises several vital steps. First, data was acquired from the literature and processed to build the required dataset. Second, equations were formulated based on the dataset using machine learning-based regression analysis. A multi-objective constrained genetic algorithm (GA) code was written to optimize the developed equations while considering multiple objectives and constraints. Following optimization, the obtained compositions were tested by simulations of a containment structure against different radiation particles using OpenMC (Open-Source Monte Carlo particle transport)[78] code. Lastly, the sustainability parameters were studied and compared.

Data acquisition and generation

Figure 1 shows most of the materials used to improve concrete's radiation shielding property against either gamma rays, neutron rays, or both. There are a number of possible combinations of different materials used to obtain an improvised composition, making it very complex to study and compare. Therefore, to eliminate such complexity and facilitate a meaningful comparison, concrete can be studied as a combination of weight-fraction of each element present in it. The chemical composition data of concrete provided in various researches was processed and converted into its elemental form. This conversion was based on the element's weight and proportion in the corresponding oxide compound. Each element oxide in the concrete was converted into the element's weight and oxygen. After processing the data, the 30 common elements found in improved radiation-

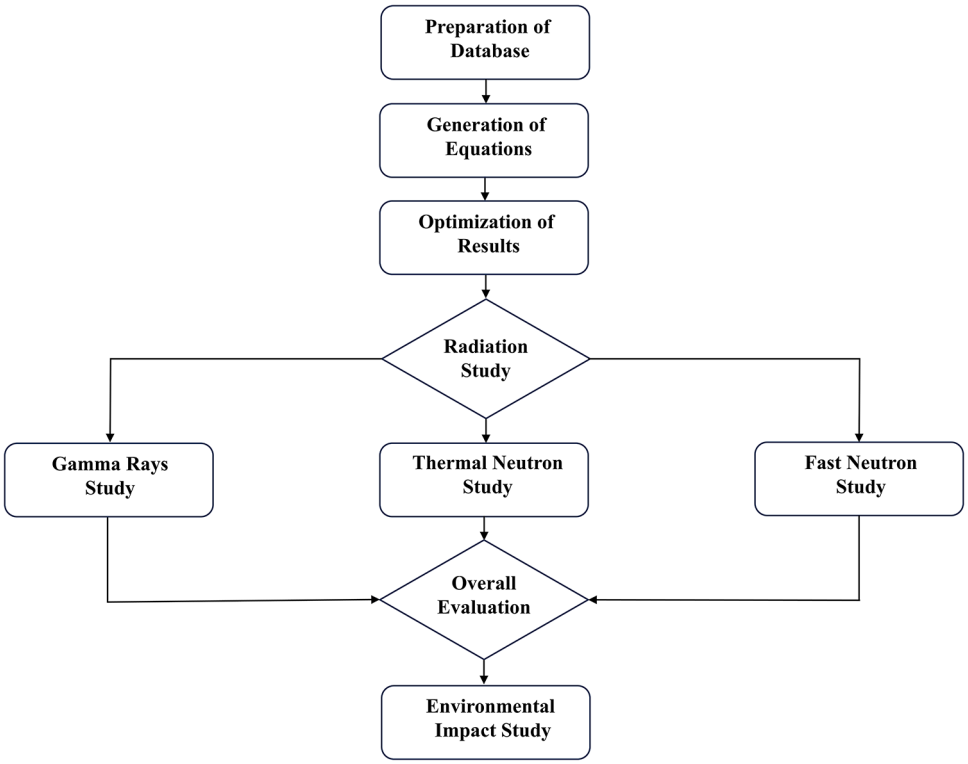


Fig. 2. Flow-Chart of the work.

shielding concrete are shown in Fig. 3. To establish a correlation between the weight fraction of each element present in the concrete composition and radiation shielding performance, a comprehensive database consisting of 495 entries was meticulously prepared. Each entry corresponds to the elemental composition of a concrete mix, considering the 30 most common elements found in radiation shielding concretes.

Radiation shielding performance can be evaluated using linear attenuation coefficient (LAC)[79]and macroscopic attenuation coefficient (MCS)[80] for gamma and neutron rays, respectively. Both LAC and MCS are characteristic properties specific to the elements present in the material and vary continuously with respect to the energy of the radiation beam. Mathematically, LAC value is defined as:

$$I = I_o . e^{-\mu x} \tag{1}$$

where 'I' is the intensity of material after passing distance 'x' in medium, 'I_o' is the initial intensity of radiation, and 'μ' is the LAC value. Conversely, MCS (Σ) is defined as:

$$\Sigma = \sigma . N \tag{2}$$

where, 'σ' is the Microscopic Cross-Section (barns) and 'N' is the Nuclei Density (Nuclei/cm^3). The radiation dose rate can also be used to evaluate the radiation shielding performance. The effective dose rate represents the potential radiation risk per unit time and is typically measured in sieverts per hour (Sv/hr). By calculating the effective dose rate at various locations beyond the shielding, radiation protection professionals can ensure that the public and workers are not exposed to unacceptable radiation levels[81].

LAC and MCS are typically obtained at a single energy point, which limits their applicability in evaluating the radiation shielding performance of concrete structures in NPPs. These structures are exposed to complex energy spectrums of gamma and neutron radiation, which vary significantly in energy and intensity. Best protection over the entire energy spectrum cannot be evaluated solely based on LAC and MCS values, as these values are highly susceptible to changes in energy. Evaluating the shielding effectiveness using LAC and MCS does not fully capture the diverse range of radiation energies in such environments. Further, the impact of radiation on the environment and human health differs for various radiation particles. By utilizing the dose rate, a more accurate and comprehensive understanding can be made of how well a concrete composition can protect against the energy spectrum of different radiation particles.

Calculation of radiation dose rate

The interaction of radiation particles with materials can be understood and simulated using various radiation particle transport codes such as FLUKA[82], GEANT4[83], and OpenMC code[78]. OpenMC is an open-source Monte Carlo computational tool designed explicitly for particle transport simulations in nuclear engineering

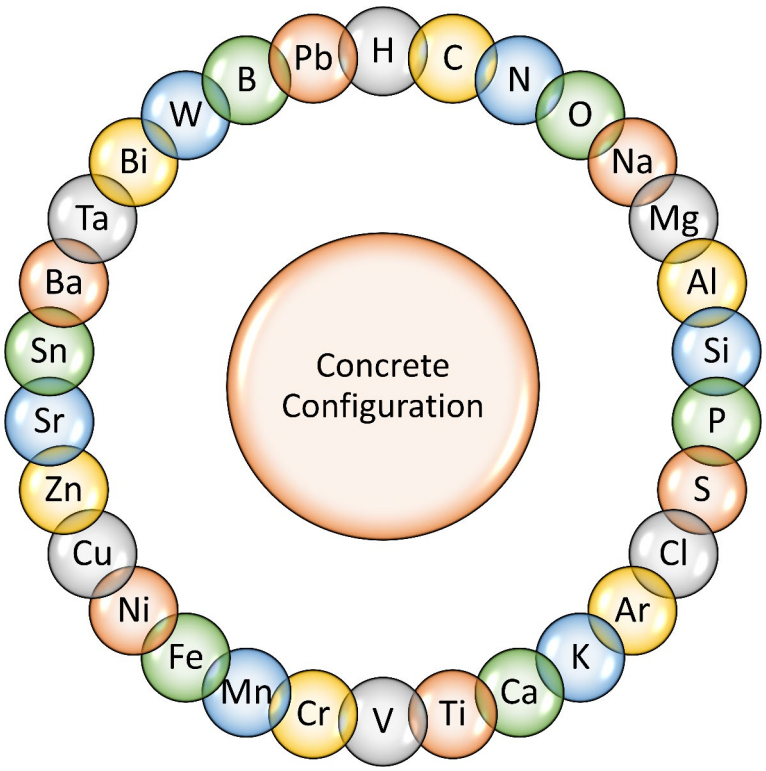


Fig. 3. Major elements used for developing radiation shielding concrete.

and radiation physics. It provides a wide range of features for simulating interactions of neutrons, gamma rays, and electrons, allowing for precise predictions of various nuclear phenomena and reactor behaviours. OpenMC allows the user to develop complex geometries using Constructive Solid Geometry (CSG) modelling technique. Using the CSG modelling technique, a three-dimensional nuclear containment structure (NCS) was modelled with half a metre thick section dimensions and a radiation source in the centre. The corresponding thickness was defined in order to capture the shielding penetration effectively. The geometrical details of the model are shown in Fig. 4.

An NCS structure is subjected to the energy spectrums of gamma rays and neutrons. Neutrons are further divided into thermal neutrons (TN) and fast neutrons (FN) based on the energy ranges[84]. In a nuclear fission reactor, Nakashima et al.[85] experimentally evaluated the gamma ray's energy spectrum around the nuclear fission reactor. It was observed that the energy distribution was continuous around the spectrum with negligible major distinctive peaks. Further, a recent study by Makii et al.[86] observed that the prompt fission gamma ray's spectra (PFGS) can extend up to 20 MeV of energy in a spontaneous fission reaction of uranium-235. Therefore, the energy distribution of gamma rays in this study was kept continuous, with a maximum energy of 20 MeV to consider all the extremities. The energy distribution of gamma rays is shown in Fig. 5(a). TN are neutrons with energy ranging between 0.025 eV to 1 eV. The energy distribution of TN was kept continuous, as shown in Fig. 5(b), covering the entire thermal energy spectrum. The energy distribution followed by FN in a nuclear fission reaction is a Gaussian distribution[87] with a mean of 2 MeV. Therefore, the Gaussian distribution was used for the simulation with the energy distribution, as shown in Fig. 5(c).

The material of the NCS was varied with different concrete compositions from the established dataset. The elemental composition of air, shown in Fig. 4, was kept at 78.441% nitrogen, 21.075% oxygen, and 0.46% argon, with a density of 0.0012 g/cc. Simulations were conducted for various concrete compositions exposed to individual gamma rays, TN, and FN sources, each characterized by their respective energy spectrum, as depicted in Fig. 5. The simulations were operated under the fixed source run mode with a specified source setting. Each batch consisted of 5000 particles, and 50 batches were executed to ensure thorough data collection and statistical robustness.

The energy spectrum corresponding to each radiation type was obtained at an outer boundary. The particle energy spectra were multiplied by the respective dose coefficient to yield a dose value. Dose coefficients can be applied in a neutronics tally using the OpenMC energy function filter. The International Commission on Radiological Protection (ICRP) recommends a four-point cubic Lagrangian interpolation formula on a log–log graph scale interpolating absorbed dose and effective dose per fluence[88]. The dose tally was expressed in units of pico sieverts square centimetres (pSv cm^2) per source particle. The tally result was divided by the surface area to convert it to pSv. Subsequently, the converted value was multiplied by the activity of the source, measured in becquerels (Bq), to obtain the effective dose rate (pSv/s). In this research, a source activity of 0.15 MBq was assumed to achieve the desired comparative results. Additionally, each fission reaction is expected to release three neutron particles and seven gamma rays particles on average[89]. These values were then used to calculate the effective dose rates for gamma rays, TN, and FN. To further enhance the authenticity of the simulation process, a multi-type particle simulation was also conducted using a defined continuous energy spectrum of different particles, allowing the Total Effective Dose Rate (TEDR) to be calculated collectively. The results from both approaches were compared and analyzed to provide a deeper understanding of radiation shielding and validation of the simulation process.

The performed evaluation resulted in the development of an extensive dataset of different concrete compositions and effective dose rates corresponding to each radiation type. The developed dataset will help us

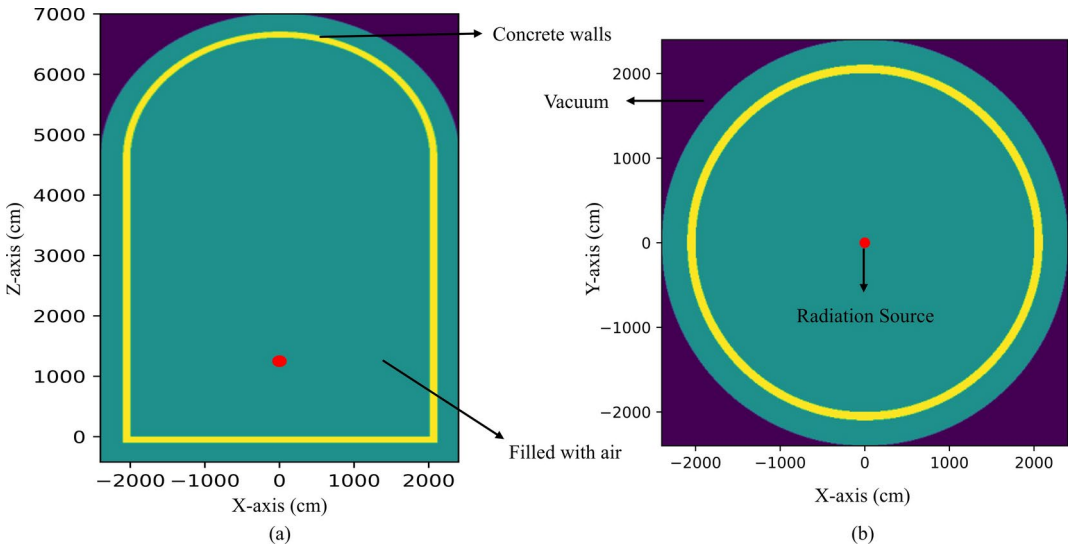


Fig. 4. Dimensions and cross-section of (**a**) Front view (**b**) Top view of the simulated NCS.

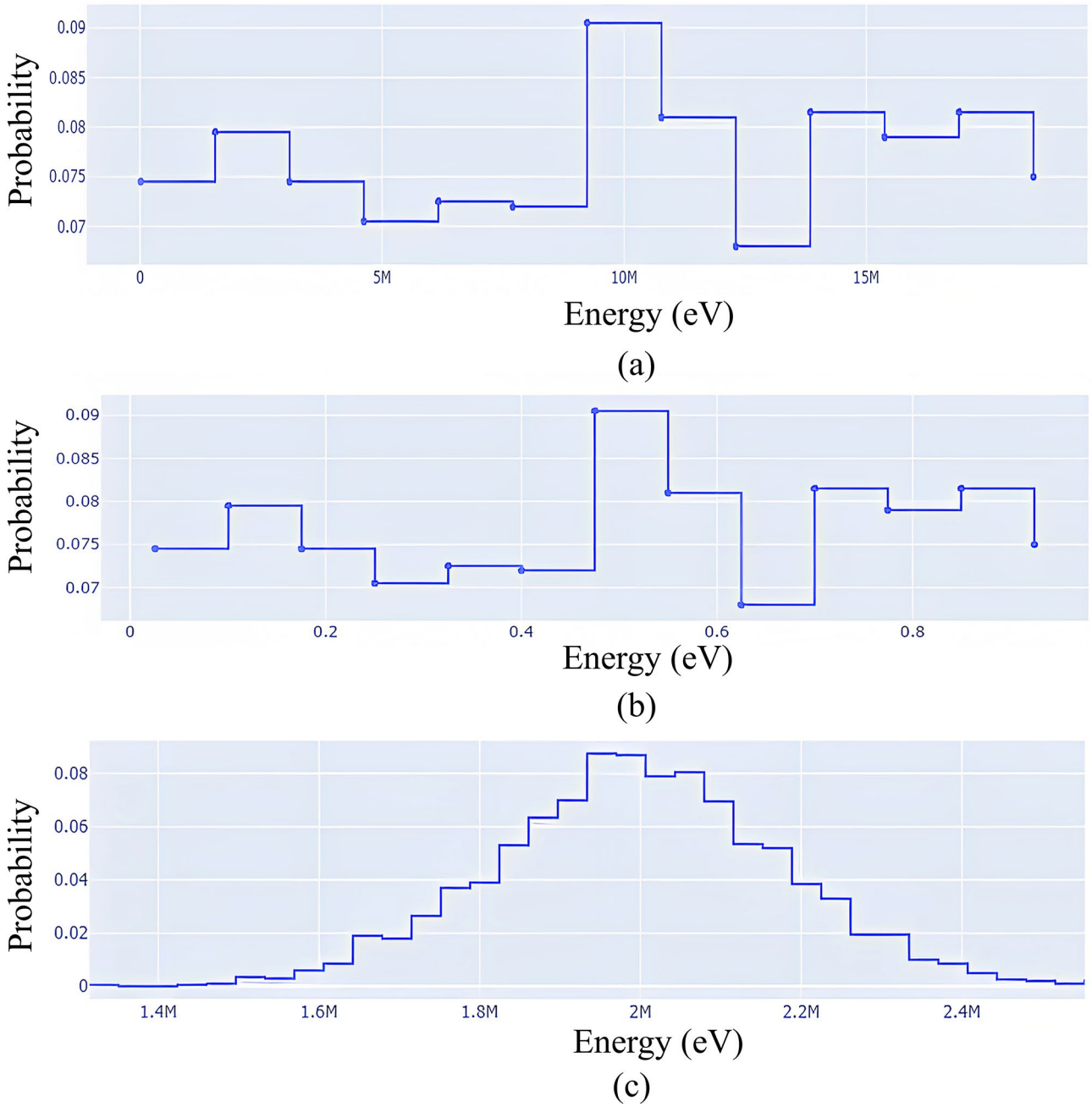


Fig. 5. Simulated energy distribution of (**a**) Gamma rays Energy, (**b**) Thermal neutrons, and (**c**) Fast neutrons.

understand the effect of individual elements present in the composition on its shielding performance against different radiation particles across a broad energy spectrum.

Generation of equations

A relationship needs to be developed between the element's weight fraction and dose rate to understand the behaviour of concrete composition on radiation shielding performance. To establish three mathematical correlations, i.e., weight fraction of each element v/s dose rate, in the case of gamma rays, TN, and FN, linear regression analysis was performed on the three datasets using the regression learner app available in MATLAB®2023[90]. Supervised machine learning algorithms and techniques are the underlying technology in the regression learner app, which helps in model selection, training, feature engineering, hyperparameter tuning, evaluation, and prediction. The models underwent training and validation using 70% of the dataset, randomly partitioned, and subsequently tested on the remaining 30% as a test set. The evaluation of prediction accuracy in these datasets relied on commonly employed performance metrics, i.e., correlation coefficient (R) and root-mean-square error (RMSE), shown in Equations 3 and 4, respectively.

$$RMSE = \sqrt{\frac{1}{n}\sum_{i=1}^{n}\left(y_i^* - y_i\right)^2} \tag{3}$$

$$R = \frac{\sum_{i=1}^{n}\left(y_i^* - \bar{y}^*\right)\left(y_i - \bar{y}\right)}{\sqrt{\sum_{i=1}^{n}\left(y_i^* - \bar{y}^*\right)^2 \cdot \sum_{i=1}^{n}\left(y_i - \bar{y}\right)^2}} \tag{4}$$

In the above equations, n is the total number of concrete compositions in the dataset, Y_i^* and Y_i are the predicted and actual dose rate values, $\overline{Y^*}$ and $\overline{Y}$ are the mean values of predictions and observations, respectively.

K-folds cross-validation technique was used to improve the quality of the developed regression model. In this, the data was split into k equal folds and the model was trained k times, with each training iteration utilizing k-1 folds of data and evaluating the remaining fold. The performance metrics were calculated for each iteration and then averaged to evaluate the model's overall performance. K value was selected as 10 in this study. This technique facilitates model selection, hyperparameter optimization, and assess how well the model will generalize to new data.

The overall statistical significance of the generated regression models was evaluated by performing the F-test on the parameters obtained in regression analysis[91]. The F-test enables us to determine if the model with all the input parameters is superior to a basic model that predicts the mean value (intercept). It compares the model sum of squares (explained variation) with the residual sum of squares (unexplained variation) and evaluates whether the variation explained is substantially greater than what would be expected by chance alone. MATLAB code was written to perform an F-test on the three linear regressed models generated in the previous step. The steps covered in performing the F-test and examining the null hypothesis[92] are shown in Fig. 6. The significance level was kept to 0.05 as a limit.

Optimization using multi-objective constrained genetic algorithm

Relationships between the element's weight fraction and effective dose rate for gamma rays, TN, and FN were established in the previous section. These can be optimized to achieve the best combination of elements and their percentage, that will provide better shielding in all three directions without compromising each other. Various techniques and algorithms for optimization are available in the literature. However, for the given problem, the GA was used as it offers advantages such as parallelism, global optimization, flexibility, and ease in handling multi-objectives and constraints[93].

A multi-objective constrained GA code was written to find the weight fraction of all 30 elements for the minimum value of dose rates in all three cases. This optimization considered all three regression equations to account for the effects of energy variation. To ensure the feasibility of the code output, the following constraints were applied:

Element constraints

Durability, strength, and production of concrete constraints the maximum and minimum quantity of elements in the concrete. The range of weight fraction of each element based on the essential requirement and element limitations of concrete were defined in this constraint. The range was decided based on previous research's maximum and minimum values. The element constraints applied in the algorithm are shown in Table 1.

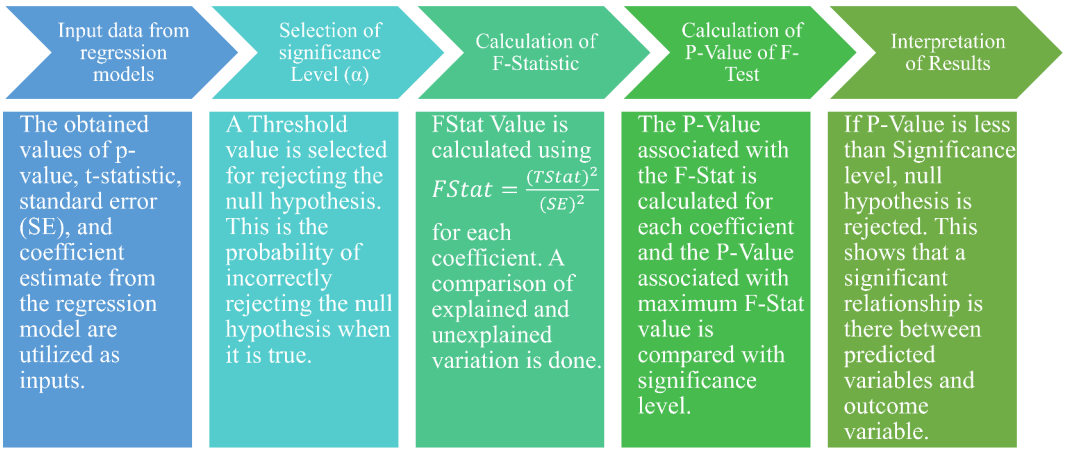


Fig. 6. F-Test procedural sequence.

Density constraints
The density of heavy radiation shielding concrete varies from 3000 kg/m^3 to 3600 kg/m^3. Therefore, to achieve feasible results, density constraint was applied, and optimized compositions were obtained for density ranges 3000–3100 kg/m^3, 3100–3200 kg/m^3, 3200–3300 kg/m^3, 3300–3400 kg/m^3, 3400–3500 kg/m^3 and, 3500–3600 kg/m^3. These variations were considered to analyse the variation of each element while considering changes in density and maintaining practicality as a critical factor.

Oxygen weight constraint
The total weight fraction of element 'O' is the sum of the weight percentage of oxygen in the oxides of other elements. A linear regulation was established to ensure an equal oxygen distribution among all the elements involved.

The optimization of elemental composition in concrete required balancing several trade-offs to ensure both effective radiation shielding and structural integrity. Heavy elements like lead and bismuth, which are crucial for enhancing shielding, had to be carefully balanced with essential structural elements such as calcium, silicon, and aluminium. Increasing the proportion of heavy elements for better shielding could compromise mechanical strength, complicate production feasibility, and reduce workability. Similarly, while optimizing for higher density, leading to improved radiation attenuation, it introduces challenges such as reduced flexibility in production and potential practical limitations in real-world applications. Managing the oxygen weight constraint was also essential, as most elements exist in oxide form, and controlling free oxygen content was necessary to maintain proper balance. Although these constraints limit the shielding performance to some degree, they are crucial to ensure that the final concrete compositions are both practical and feasible for radiation shielding applications.

In the code developed, three input functions were taken with zero tolerance. The population size of 1000 with a maximum of 500 generations was considered in the code. The convergent solutions obtained after applying GA and the constraints were compared and evaluated using the Pareto Dominance Relationship (PDR). PDR helps in determining whether solutions are dominated by one another in case of possible conflicts between multiple objectives. In this process, non-dominating solutions are sacrificed to increase the algorithm's effectiveness and deal with conflicting goals. Three-dimensional pareto-optimality curves were plotted to understand the optimal solutions in the decision space and identify the desirable solutions.

Radiation analysis using OpenMC code

The effectiveness of the optimized compositions generated from the GA code must be inspected against gamma and neutron rays over the defined energy spectrums to consider all the aspects. Using OpenMC code, the interaction between matter and gamma rays, TN, and FN were analysed separately.

Gamma rays simulation
Gamma rays are a form of high-energy electromagnetic radiation with the electromagnetic spectrum's shortest wavelengths and highest frequency. They are produced through nuclear processes, such as radioactive decay and nuclear fission reactions. Due to their tremendous energy, gamma rays have exceptional penetrating abilities[94]. Therefore, it is necessary to provide shielding against gamma rays due to their high penetration and possible threat. A wide range of possible interactions can occur when gamma rays come in contact with matter, as shown in Fig. 7. These interactions are random and depend on the matter's specific properties and the gamma rays's energy. As a result, the outcome of any interaction is probabilistic in nature. Uncertainties and the stochastic nature of material-particle interaction can be addressed with the help of Monte Carlo simulations. Therefore, OpenMC code was used to simulate the transport of neutrons and gamma rays through materials.

An NCS structure generally consists of concrete sections in a range of one-metre thickness[95]. The NCS model, shown in Fig. 4, was modified with a one-metre thickness to understand the behaviour of various compositions and their efficiency in shielding. The energy distribution of gamma rays has already been shown in Fig. 5(a). Simulations were performed to obtain the flux leakage and effective dose rate for different concrete compositions and those available in the literature. The secondary gamma rays, generated through Compton scattering, pair production, or photoelectric absorption, were also considered while calculating the tallies. A comparative study was conducted to evaluate the efficiency of the optimized concrete compositions quantitatively with the inclusion of associated probabilities. To keep the structure's resilience in check, just like the factor of safety, an additional command of "survival biasing" being true was added to the code.

Neutron rays simulation
Neutrons are zero-charged particles found in the nucleus of an atom alongside protons. They play a crucial role in nuclear fission reactions as they can initialize a reaction, be released as a product, and produce chain reactions.

Elements	H	C	N	O	Na	Mg	Al	Si	P	S	Cl	Ar	K	Ca	Ti
Max %	2	2	1	54	2	18	50	35	5	5	16	0	2	30	7
Min %	0.6	0	0	31	0	0	0.6	8	0	0	0	0	0	8	0
Elements	**V**	**Cr**	**Mn**	**Fe**	**Ni**	**Cu**	**Zn**	**Sr**	**Sn**	**B**	**Ta**	**Bi**	**W**	**Ba**	**Pb**
Max %	1	2	0.5	46	3	0.4	0.7	1	0.1	44	0.1	22	19	16	3
Min %	0	0	0	0	0	0	0	0	0	0	0	0	0	0	0

Table 1. Maximum and Minimum values constraints on each element for results viability.

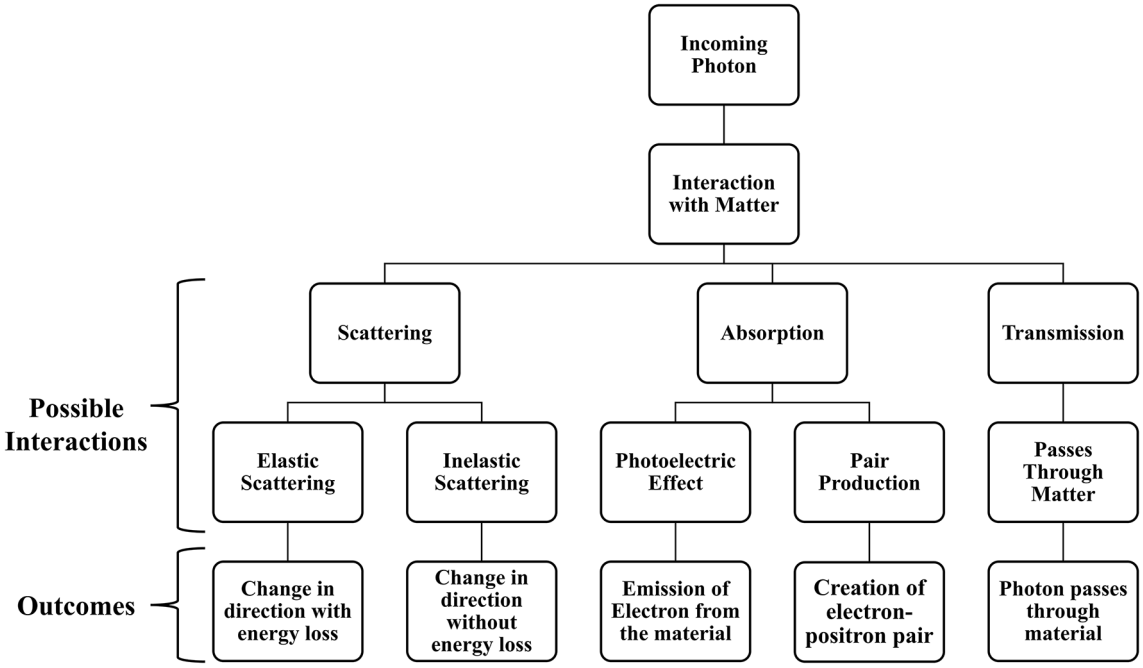


Fig. 7. Possible gamma rays-matter interaction.

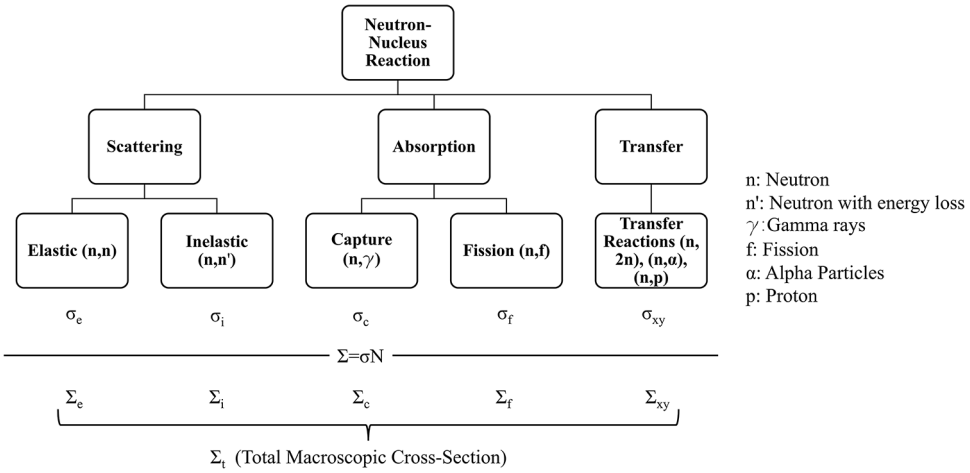


Fig. 8. Possible neutron-matter interactions.

The possible neutron interactions with a nucleus are shown in Fig. 8. MCS of several additional elements in the targeted concrete compositions were plotted and compared over the energy range, as shown in Fig. 9. From the graph plotted, it is quite visible that different elements show better behaviour in different energy ranges. Therefore, the study is further bifurcated based on the energy ranges of neutrons to include the variation of element v/s neutron energy into the scope of this work.

Thermal neutron simulation TN has energies corresponding to the environment's temperature and plays a crucial role in nuclear fission reactions. An NCS, as shown in Fig. 4, with a 1 m thick cross-section was simulated. The energy distribution of the thermal neutron was kept continuous, as shown in Fig. 5(b). Simulations were performed to obtain the TN flux and dose tally of the optimized concrete compositions and the best compositions from the literature. Considering the survival biasing being true, TN flux leakage of the NCS was obtained and compared for all the compositions.

Fast neutron simulation Neutrons with high kinetic energy ranging over 1 MeV are called FN. These neutrons are generated during nuclear fission reactions and show high penetrations to matter, including lead. The Gaussian distribution was used for the simulation with the energy distribution, as shown in Fig. 5(c). A similar NCS,

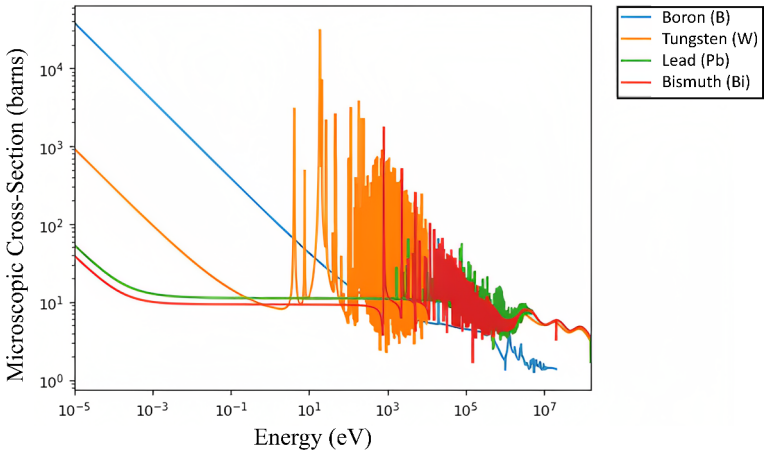


Fig. 9. Total microscopic cross-section v/s energy of neutron of few additional elements.

as discussed before, was simulated with the fast neutron as an energy source. Neutron interactions with matter can also produce secondary particles, including gamma rays, protons, alpha particles, and additional neutrons. In the default settings of the OpenMC code, tallies for secondary particles generated during neutron interactions are not calculated. To address this, the default configuration was modified by enabling the "photon_transport" option, allowing the evaluation of secondary gamma rays produced during neutron interactions with matter. Once enabled, gamma rays flux and current tallies were defined alongside neutron tallies at the outer surface. However, the contribution of secondary gamma rays at the surface was found to be minimal, accounting for only about 0.6% of the neutron dose rates at their maximum. As a result, only neutron flux and dose measurements were primarily considered, as they represent the most significant contribution to overall radiation shielding effectiveness. For reference, the EDR values of secondary gamma rays released during the interaction of neutron with matter have been presented in Table S1. Rest assured, all the parameters were kept the same, and flux leakage and radiation dose rates were obtained.

Overall evaluation of radiation shielding performance

The overall radiation performance of the concrete compositions can be evaluated and compared based on the TEDR value. An effective dose rate helps compare all the radiation particles on the same scale. Therefore, this approach provides a comprehensive measure of the shielding capabilities of various concrete compositions against different types of radiation. The effective dose rates were obtained individually for gamma rays, TN, and FN. The summation of all the effective dose rate values is a measure of TEDR. The value of TEDR was obtained for the proposed concrete compositions and compared with the compositions available in the literature to evaluate the overall shielding performance over the defined energy spectrum.

Assessment of long-term sustainability of the proposed composition

As the world is moving towards sustainable development goals, it is essential to understand the effects of every proposed composition or structure on the environment. The sustainability of a product, material, or configuration can be quantified by measuring the Global Warming Potential (GWP). GWP estimates the emissions from both the production processes, including raw material extraction and manufacturing, as well as the transportation phase, which accounts for the emissions from moving raw materials and finished products. By considering all stages, from production to transport and disposal, GWP provides a comprehensive view of the environmental impact associated with a product or process.

To assess the sustainability of optimized concrete composition, an NCS structure was simulated with optimized concrete composition and conventional concrete composition. The composition of conventional concrete considered in this research is 380 kg/m^3 cement, 750 kg/m^3 sand, 1345 kg/m^3 coarse aggregates, and 152 kg/m^{3}water[48]. The wall thickness of the NCS was varied to achieve the equivalent performance level of the best concrete composition developed against all the radiations. The GWP of all the construction materials (cement, fine natural aggregates (FNA), coarse natural aggregates (CNA))[96], and metals[97]are provided in the literature. Due to data availability constraints, it was assumed that the GWP values of metals closely approximate those of their oxides. This is a conservative but practical assumption, as the GWP of refined metals is typically higher than that of their oxide forms due to the additional energy-intensive refining processes[97]. GWPs of the materials required per cubic meter for the mix design of the required concrete composition, along with the additional element oxides, are shown in Table 2.

The results of the optimum concrete composition were defined in elemental oxide form. The defined elemental composition can be achieved using different possible material combinations depending on the choice. A sample mix design was assumed to calculate the GWP, considering the elemental weight fraction of the proposed optimum composition. Using the GWP data, the GWP for developing the required concrete per cubic meter was calculated. In both cases, the material required for developing the NCS was calculated, and the overall GWP was calculated for developing the required structure at a given performance level.

Material name	Cement	Water	FNA	CNA	Iron oxide (Fe_2O_3)	Nickel oxide (NiO)	Boron oxide (B_2O_3)	Tungsten oxide (WO_3)
GWP (kg CO_2-eq/kg)	315	0.02	7.53	33.3	1.5	6.5	1.5	12.6

Table 2. Global Warming Potential (GWP) (kg CO_2-eq/kg) values of materials required for improvised concrete production.

x_1	x_2	x_3	x_4	x_5	x_6	x_7	x_8	x_9	x_{10}	x_{11}	x_{12}	x_{13}	x_{14}	x_{15}
H	C	N	O	Na	Mg	Al	Si	P	S	Cl	Ar	K	Ca	Ti
x_{16}	x_{17}	x_{18}	x_{19}	x_{20}	x_{21}	x_{22}	x_{23}	x_{24}	x_{25}	x_{26}	x_{27}	x_{28}	x_{29}	x_{30}
V	Cr	Mn	Fe	Ni	Cu	Zn	Sr	Sn	B	Ta	Bi	W	Ba	Pb

Table 3. Variable names representing each element.

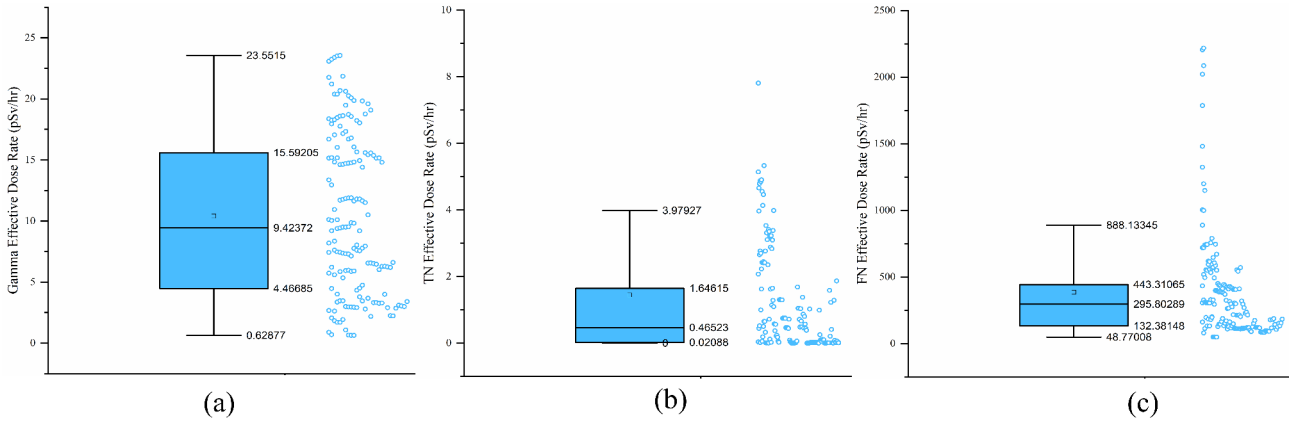


Fig. 10. EDR values of (**a**) gamma, (**b**) TN, and (**c**) FN values for different concrete compositions.

Results and discussions

Results corresponding to each task performed are discussed in this section:

Generation of equations

Each element's weight fraction was assigned to a variable name, as shown in Table 3.

Regression learner app available in MATLAB®2023, based on supervised machine learning, develop a linear predictive model with high predictive accuracy. The developed models were based on the calculated dose rate values of different concrete compositions, as shown in Fig. 10. The format of the equation is shown in Equation 5**,** where 'ϵ' represents the error associated with the model. The results of performed linear regressions on three energy ranges are shown in Table 4.

$$Dose\ rate\left(pSv/hr\right) = \sum_{i=1}^{30} \alpha_{i-1} x_i + c + \in \tag{5}$$

The performance of the generated equations was evaluated by plotting the predicted v/s true response for the training and test data, as shown in Fig. 11.

The RMSE and R-squared values were obtained to evaluate the goodness of fit. The correlation value (R) in the case of training data was obtained as 0.9055, 0.9539, and 0.9219 for gamma rays, TN, and FN, respectively. For the test data, the values were 0.9592, 0.9539, and 0.9327 for gamma rays, TN, and FN, respectively. The high correlation coefficients on the training and test set indicate the model's strong predictive capability. Additionally, the very low RMSE values for the training and test sets suggest that the model did not suffer from overfitting. Based on the developed plots and evaluating parameters, it is evident that the linear relationship between each element's weight fraction and the effective dose rate represents a good fit. Further, the overall significance of the models was evaluated by performing F-tests on the statistics parameters, shown in Table 4. The null hypothesis was "rejected" in all three models, which validated the overall statistical significance of all three linear regression models.

	Regression Results (Gamma rays (pSv/hr))				Regression Results (TN (pSv/hr))				Regression Results (FN (pSv/hr))			
	Estimate	SE	TStat	P-value	Estimate	SE	TStat	P-value	Estimate	SE	TStat	P-value
Intercept	52.92642	3.251073	16.27968	7.43E-28	5.653168	1.174856	4.811797	6.42E-06	785.9143	207.104	3.794781	0.000276
α_0	−0.03414	0.004557	−7.49119	5.92E-11	−0.01418	0.001807	−7.85022	1.13E-11	−1.8949	0.329678	−5.74772	1.38E-07
α_1	0.031581	0.008593	3.675142	0.000415	0.011307	0.004365	2.590177	0.011286	−0.96534	0.527745	−1.82919	0.070878
α_2	−0.01671	0.003411	−4.89907	4.55E-06	−0.00189	0.001597	−1.18342	0.239942	0.118311	0.243706	0.485467	0.628594
α_2	−0.01176	0.001246	−9.43754	7.03E-15	−0.00096	0.000589	−1.62635	0.107577	−0.22514	0.0766	−2.93919	0.004236
α_4	−0.10362	0.029152	−3.55447	0.000621	−0.02578	0.013588	−1.89707	0.061214	−2.29868	1.823618	−1.2605	0.210937
α_5	0.00612	0.011439	0.535027	0.594028	−0.00219	0.006235	−0.35111	0.726377	−1.32708	0.717167	−1.85045	0.067723
α_6	−0.01501	0.001627	−9.22524	1.89E-14	−2.2E-05	0.0006	−0.03611	0.971275	−0.30312	0.116935	−2.59219	0.011225
α_7	−0.01204	0.002554	−4.71522	9.37E-06	0.000961	0.000841	1.142884	0.256296	−0.18501	0.164846	−1.12233	0.264882
α_8	0.082867	0.177172	0.467719	0.641183	0.003429	0.004066	0.843153	0.401509	−1.45622	0.500086	−2.91195	0.004587
α_9	−0.03452	0.005525	−6.24761	1.59E-08	0.003537	0.003921	0.902088	0.369559	0.699127	0.382983	1.825478	0.071441
α_{10}	0.306569	0.154834	1.979991	0.05094	0.056075	0.086215	0.6504	0.517188	−13.5286	9.584988	−1.41143	0.161767
α_{11}	0	0	0	0	0	0	0	0	0	0	0	0
α_{12}	0.05569	0.023375	2.382446	0.019429	0.008108	0.01119	0.724583	0.470698	0.574134	1.469471	0.390708	0.696991
α_{13}	−0.03028	0.002503	−12.0997	3.52E-20	−0.00523	0.001165	−4.48447	2.27E-05	0.213986	0.14879	1.438177	0.154056
α_{14}	−0.01117	0.00421	−2.65423	0.009487	0.002107	0.001786	1.17972	0.241403	−0.05139	0.251005	−0.20474	0.838266
α_{15}	−7.04918	6.590466	−1.0696	0.287826	−3.45317	3.076798	−1.12233	0.264884	−289.064	455.7517	−0.63426	0.527616
α_{16}	−0.02941	0.085603	−0.34353	0.732051	−0.0451	0.048582	−0.92824	0.355912	−8.80264	5.074287	−1.73475	0.086409
α_{17}	−0.0721	0.02752	−2.61986	0.010417	−0.00212	0.008562	−0.24807	0.804675	−2.94624	1.276565	−2.30795	0.023432
α_{18}	−0.01537	0.000945	−16.2602	8.02E-28	−0.0018	0.000335	−5.39277	6.13E-07	0.000523	0.053	0.009872	0.992147
α_{19}	−2.23254	0.953479	−2.34146	0.021548	−0.39412	0.539436	−0.73062	0.467018	86.59829	58.72823	1.47456	0.144025
α_{20}	0.024225	0.123249	0.19655	0.844649	−0.02432	0.056932	−0.42722	0.670297	−4.91409	7.795423	−0.63038	0.530136
α_{21}	0.024576	0.062184	0.39521	0.693678	0.002544	0.025278	0.100655	0.920062	0.051673	3.93384	0.013136	0.98955
α_{22}	−0.03609	0.035986	−1.00292	0.318747	0.005517	0.015445	0.357231	0.721804	4.86298	2.8713	1.693651	0.093993
α_{23}	−63.0547	46.00002	−1.37075	0.174061	18.3157	20.64783	0.887052	0.377554	−1591	3101.972	−0.5129	0.609352
α_{24}	−0.01327	0.001568	−8.46149	6.64E-13	0.002716	0.001112	2.442472	0.016658	0.50327	0.095954	5.244885	1.13E-06
α_{25}	285.8862	131.5622	2.173012	0.032562	−31.2976	56.82937	−0.55073	0.583264	7803.522	8782.918	0.888488	0.376785
α_{26}	−0.19705	0.077407	−2.54564	0.012712	−0.03013	0.042162	−0.71454	0.476853	9.660343	4.776879	2.022313	0.046288
α_{27}	−0.04029	0.002702	−14.9105	1.91E-25	−0.00744	0.001141	−6.51976	4.79E-09	0.804242	0.193523	4.15579	7.70E-05
α_{28}	−0.05591	0.003834	−14.5818	7.52E-25	−0.01223	0.001918	−6.37596	9.05E-09	0.59943	0.264016	2.270435	0.02571
α_{29}	−0.04503	0.007839	−5.74446	1.40E-07	−0.00163	0.006339	−0.25787	0.797134	1.085195	0.442081	2.454742	0.016138

Table 4. Posterior statistics of parameters of developed regression models.

Optimization using multi-objective constrained genetic algorithm

Three developed equations were processed through GA to give six different concrete compositions in different density ranges with the best shielding properties. The variation of density ranges was considered to keep the possible deviations into the picture that might occur while developing the concrete in real life. Three-dimensional pareto-optimality curves were plotted for all six density ranges to review the convergence and obtain the best results in possible conflicts between results. The plotted curves are shown in Fig. 12. The scattered plots from the Pareto curves follow the required convergence trend in a three-dimensional plane. From this, it can be depicted that the three equations, along with all the constraints, converge to the most optimum solution for a given density range of concrete. The results of the optimized concrete compositions in different density ranges are shown in Table 5, 6, 7, 8, 9, 10.

Results from the code also align with the already known concepts about these elements. It has already been discussed before that different elements showcase superior shielding performance against different radiation particles in different energy ranges. The right balance between low and high atomic number elements is required for the best overall radiation shielding. It is already known that boron is highly effective against TN, whereas tungsten and iron are effective against high-energy neutrons and gamma rays. The results from the code show that these three additional elements at a given weight fraction will provide the highest overall shielding. Density also plays an important role and in the given density range, code always converged to the highest density. The density of the output composition came out to be 3100 kg/m^3, 3200 kg/m^3, 3300 kg/m^3, 3400 kg/m^3, 3500 kg/m^3, and 3600 kg/m^3 respectively in their density ranges. Although the generated data is in the form of the optimum elemental composition of the concrete, it gives a clear picture of the quantity of addition of the new materials and the corresponding modifications in the conventional concrete's mix-design as per the requirement and suitability of the different forms of additional materials.

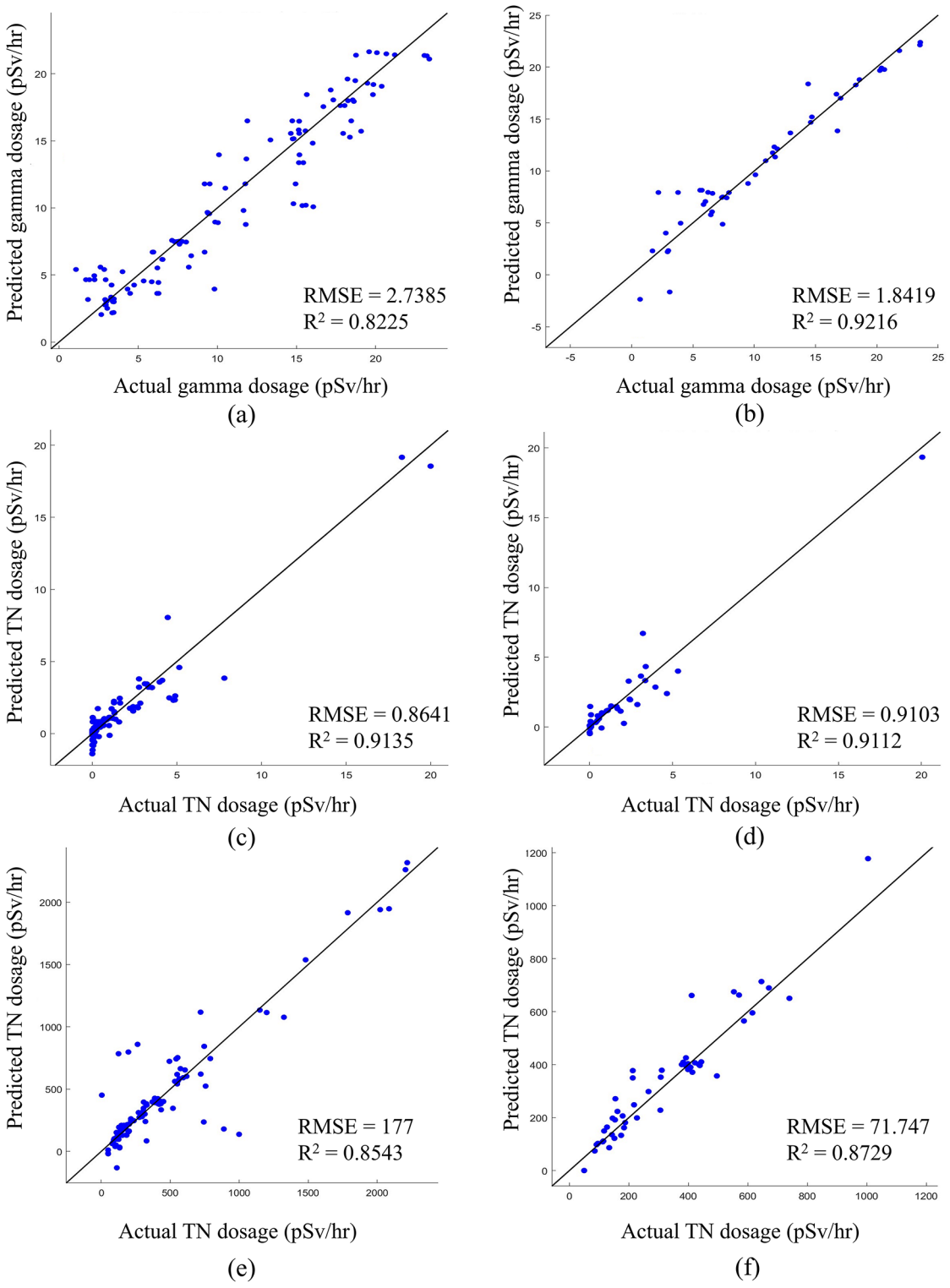


Fig. 11. Predicted -v/s- actual response of developed regression models training dataset of (**a**) gamma rays, (**c**) TN, and (**e**) FN, respectively and test dataset of (**b**) gamma rays, (**d**) TN, and (**f**) FN, respectively.

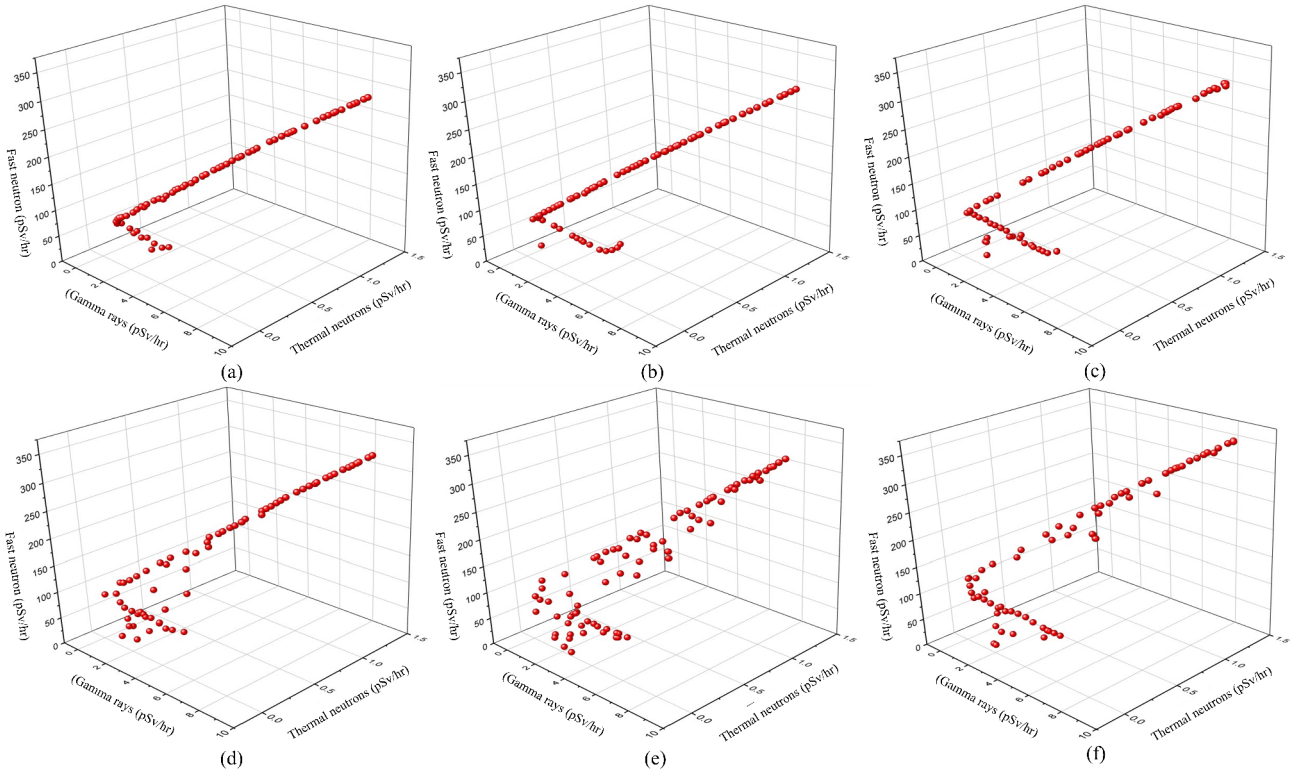


Fig. 12. Pareto-optimality curves obtained from GA algorithm code for density ranges (**a**) 3000–3100 kg/m^3 (**b**) 3100–3200 kg/m^3 (**c**) 3200–3300 kg/m^3 (**d**) 3300–3400 kg/m^3 (**e**) 3400–3500 kg/m^3 (**f**) 3500–3600 kg/m^3.

Elements	H	C	N	O	Na	Mg	Al	Si	P	S	Cl	Ar	K	Ca	Ti
Wt. (kg)	18.6	0	0	1825.9	0	0	18.6	241.8	0	0	0	0	0	241.8	0
Elements	**V**	**Cr**	**Mn**	**Fe**	**Ni**	**Cu**	**Zn**	**Sr**	**Sn**	**Ba**	**Ta**	**Bi**	**W**	**B**	**Pb**
Wt. (kg)	0	0	0	219.79	46.5	0	0	0	0	0	0	0	93	393.7	0

Table 5. Optimized Concrete Composition for Density range (3000–3100 kg/m^3).

Elements	H	C	N	O	Na	Mg	Al	Si	P	S	Cl	Ar	K	Ca	Ti
Wt. (kg)	19.2	0	0	1884.8	0	0	19.2	249.6	0	0	0	0	0	249.6	0
Elements	**V**	**Cr**	**Mn**	**Fe**	**Ni**	**Cu**	**Zn**	**Sr**	**Sn**	**Ba**	**Ta**	**Bi**	**W**	**B**	**Pb**
Wt. (kg)	0	0	0	226.9	48	0	0	0	0	0	0	0	96	406.4	0

Table 6. Optimized Concrete Composition for Density range (3100–3200 kg/m^3).

Elements	H	C	N	O	Na	Mg	Al	Si	P	S	Cl	Ar	K	Ca	Ti
Wt. (kg)	19.8	0	0	1943.7	0	0	19.8	257.4	0	0	0	0	0	257.4	0
Elements	**V**	**Cr**	**Mn**	**Fe**	**Ni**	**Cu**	**Zn**	**Sr**	**Sn**	**Ba**	**Ta**	**Bi**	**W**	**B**	**Pb**
Wt. (kg)	0	0	0	233.9	49.5	0	0	0	0	0	0	0	99	431.8	0

Table 7. Optimized Concrete Composition for Density range (3200–3300 kg/m^3).

Elements	H	C	N	O	Na	Mg	Al	Si	P	S	Cl	Ar	K	Ca	Ti
Wt. (kg)	20.4	0	0	2002.6	0	0	20.4	265.2	0	0	0	0	0	265.2	0
Elements	**V**	**Cr**	**Mn**	**Fe**	**Ni**	**Cu**	**Zn**	**Sr**	**Sn**	**Ba**	**Ta**	**Bi**	**W**	**B**	**Pb**
Wt. (kg)	0	0	0	241.06	51	0	0	0	0	0	0	0	102	431.8	0

Table 8. Optimized Concrete Composition for Density range (3300–3400 kg/m^3).

Elements	H	C	N	O	Na	Mg	Al	Si	P	S	Cl	Ar	K	Ca	Ti
Wt. (kg)	21	0	0	2061.5	0	0	21	273	0	0	0	0	0	273	0
Elements	**V**	**Cr**	**Mn**	**Fe**	**Ni**	**Cu**	**Zn**	**Sr**	**Sn**	**Ba**	**Ta**	**Bi**	**W**	**B**	**Pb**
Wt. (kg)	0	0	0	248.15	52.5	0	0	0	0	0	0	0	105	444.5	0

Table 9. Optimized Concrete Composition for Density range (3400–3500 kg/m^3).

Elements	H	C	N	O	Na	Mg	Al	Si	P	S	Cl	Ar	K	Ca	Ti
Wt. (kg)	21.6	0	0	2120.4	0	0	21.6	280.8	0	0	0	0	0	280.8	0
Elements	**V**	**Cr**	**Mn**	**Fe**	**Ni**	**Cu**	**Zn**	**Sr**	**Sn**	**Ba**	**Ta**	**Bi**	**W**	**B**	**Pb**
Wt. (kg)	0	0	0	255.24	54	0	0	0	0	0	0	0	108	457.2	0

Table 10. Optimized Concrete Composition for Density range (3500–3600 kg/m^3).

Gamma rays simulation

The gamma rays flux contours were plotted based on the changes in flux intensity after the possible interactions with the concrete walls for different concrete compositions. The developed plots are shown in Fig. 13. From Fig. 13, it is evident that all six concrete compositions show equivalent or better attenuation properties than the best compositions in the literature. The quantitative estimation of the mean and standard deviation of flux for different concrete compositions is shown in Fig. 14. The results indicate that the shielding performance against gamma rays improves as the density increases. Compared to the available literature, the concrete_5 and concrete_6 compositions demonstrated higher flux reduction in most cases. However, the configurations presented by Sayyed et al.[27] and Luo et al.[40] outperformed concrete_5 and concrete_6 in gamma-ray shielding by a slight margin. This slight difference in shielding performance is acceptable, given that the developed compositions are designed to provide the highest overall radiation shielding. Therefore, they must balance shielding effectiveness between gamma and neutron rays, which have contrasting properties and require different considerations for optimal protection.

For facilities predominantly exposed to gamma radiation, such as healthcare centers and nuclear fuel storage units, the concrete compositions developed by[27] and Luo et al.[40] will offer a more tailored solution due to their marginally superior gamma-ray attenuation capabilities. In such environments, neutron radiation is either absent or of negligible concern; therefore, shielding against gamma rays released from radio-active materials used in medical radiology, radiotherapy, or stored in storage containers becomes a critical factor. This targeted approach allows for a more efficient design of shielding barriers, especially in environments where the interaction mechanisms of neutron radiation do not need to be factored into the composition of the concrete.

Thermal neutrons simulation

Contour plots associated with TN flux leakage are shown in Fig. 15. The mean and associated standard deviation of TN flux leakage against different compositions were obtained from the simulations performed, and the results are shown in Fig. 16. The developed contours and graphical representation of flux leakage show that all six developed concrete compositions show equivalent or better radiation attenuation properties than the rest. Additionally, all six proposed compositions demonstrated superior shielding performance, with minimal flux leakage against TN. The high performance against TN results from the presence of boron and the rightful amount of low atomic mass elements such as hydrogen, boron, silica, and calcium.

The concept of contrasting behaviour discussed earlier in the interaction of different radiation with matter is quite visible in the composition given by Sayyed et al.[27] and Luo et al.[40]. The composition provided by the researchers exhibited better performance level against gamma rays than the optimized compositions. Conversely, the performance decreased significantly against TN, resulting in very high TN flux leakage.

Fast neutrons simulation

Contour plots associated with FN flux leakage are shown in Fig. 17. From the results obtained, it can be said that none of the compositions are sufficient to restrain the FN flux from leaking out.

To understand the leakage in a quantified way, a graph was plotted with the mean and standard deviations associated with the FN flux leakage for different concrete compositions and is shown in Fig. 18. The contour plots and graphical representations demonstrate that all the developed compositions exhibit superior radiation

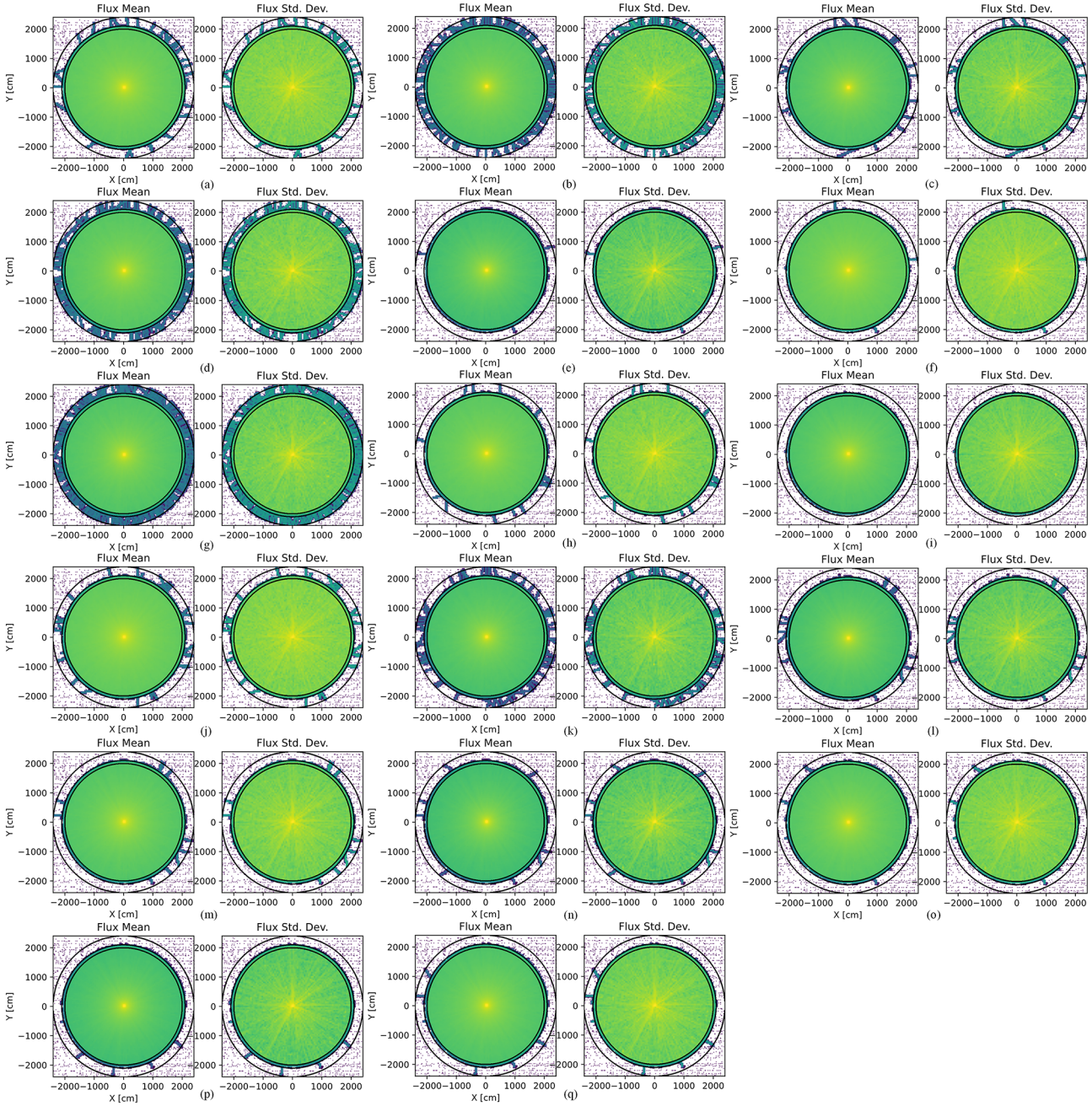


Fig. 13. Flux mean and flux standard deviation of gamma rays' interaction with different concrete compositions (**a**) Dez (**b**) Esf (**c**) Gha(**d**) Gun (**e**) Kum (**f**) Luo (**g**) Mad (**h**) Nik (**i**) Say (**j**) Suw (**k**) Zey (**l**) Concrete_1 (**m**) Concrete_2 (**n**) Concrete_3 (**o**) Concrete_4 (**p**) Concrete_5 and (**q**) Concrete_6 (where the given acronyms represent the configurations by (a) Dezampanah et al.[52] (b) Esfahani et al.[37] (c) Gharieb et al.[19] (d) Gunoglu et al.[21] (e) Kumar et al.[39] (f) Luo et al.[40] (g) Madej et al.[45] (h) Nikbin et al.[60] (i) Sayyed et al.[27] (j) Suwanmaneechot et al.[64] (k) Zeyad et al.[33] respectively.

shielding performance against FN. The composition by Dezampanah et al.[52] achieved the minimum flux leakage fraction when compared with the other compositions in the literature. However, the proposed concrete_6 composition further reduced flux leakage by 51.4% compared to the Dezampanah et al.[52] composition.

Overall evaluation of the shielding performance

Based on the flux data, it is visible that the proposed compositions are able to maintain the balance between shielding performance against the three radiation types to achieve the highest overall radiation shielding. For reference, the mean and standard deviations associated with flux leakage have been shown in Table S2. However, because flux-to-dose conversion factors vary significantly for different radiation types, the overall evaluation of shielding performance was considered based on the TEDR.

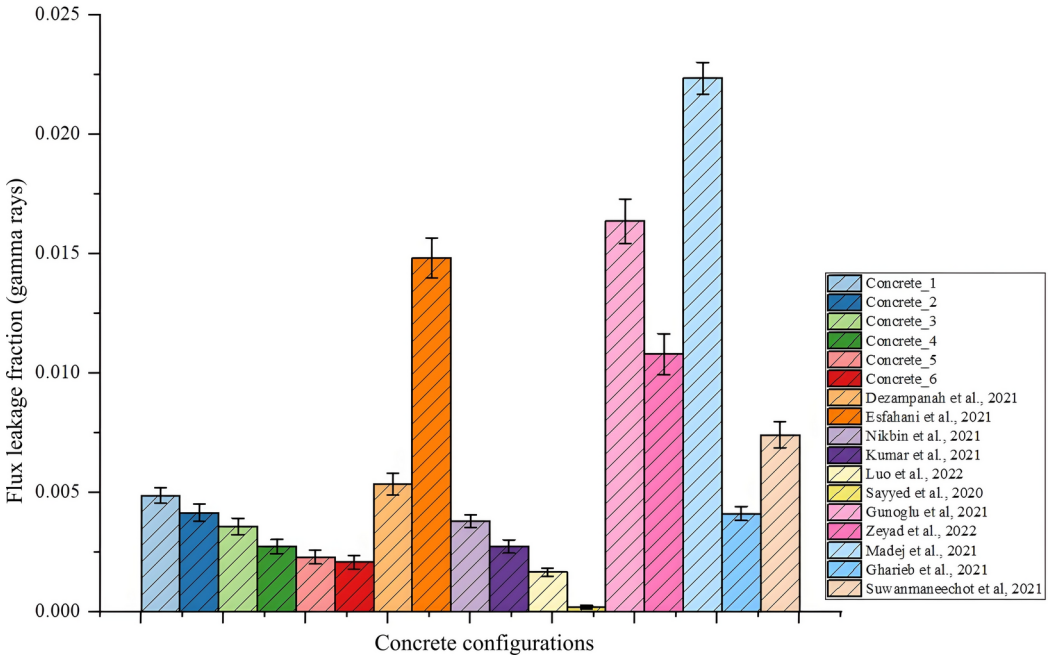


Fig. 14. Mean and standard deviation of gamma rays flux leakage fraction for different compositions of concrete.

The effective dose rates corresponding to each radiation type, i.e., gamma rays, TN, and FN, were evaluated and summed up to obtain the TEDR. The TEDR values were also determined using the multi-type particle simulation process. A comparison of the results from the two processes is presented in Table S3. The findings indicate that both approaches yield highly consistent results across all considered compositions, with a maximum variation of only 1.7%. This minor variation can be attributed to uncertainties inherent in material-particle interactions. The close agreement between the two methods underscores the robustness and reliability of both approaches in accurately evaluating TEDR values. However, the approach focusing on individual particle interactions was prioritized as it offers a more detailed understanding, making it more suitable for the objectives of the study.

The graphical representation of the TEDR for all concrete compositions is plotted and shown in Fig. 19.

The plot illustrates that the overall shielding performance of the proposed concrete_5 and concrete_6 compositions is the highest. The highest performance by the existing concrete composition was given by Dezampanah et al.[52], with a TEDR value of 54.476 pSv/hr. Compared to this, the values achieved in the concrete_5 and concrete_6 composition were 47.331 pSv/hr and 39.908 pSv/hr, respectively. Further, concrete_4 composition resulted in a TEDR value of 56.291 pSv/ hr, which is close enough to the value in the case of the Dezampanah et al.[52] composition. However, the density of concrete_4 composition is 3400 kg/m^3, whereas the density of Dezampanah et al.[52] composition was 3532 kg/m^3. Therefore, with the application of concrete_4 composition, the overall performance equivalent to the best composition in literature can be achieved with lower density levels. Moreover, the overall performance can be increased above Dezampanah et al.[52] composition by 13.12% and 26.74% with the application of concrete_5 and concrete_6 composition, respectively. Thus, the proposed compositions find the right balance between two extreme points with consideration of the dosage factors and showcase the highest overall radiation shielding. Overall, the proposed compositions will not only enhance shielding performance but will also reduce material usage and improve structural efficiency, representing a major advancement in developing next-generation NCS materials. Their ability to achieve superior performance with reduced density and greater reliability will also position them as ideal candidates for modern nuclear shielding systems.

It should be noted that while the geometry and size of NCS will affect the absolute values of radiation flux leakage, the optimization process for concrete compositions remains robust across different scales. The performance comparison of different concrete compositions is based on equivalent volumetric units, ensuring that the optimized compositions retain their relative effectiveness regardless of structural size or thickness. Therefore, while scaling may influence the total radiation leakage, the relative shielding performance of the proposed concrete compositions remains consistent, making the results applicable to a range of NCS configurations.

Assessment of long-term sustainability of the proposed composition

Simulations of the NCS made of conventional concrete and concrete_6 composition were performed to achieve zero flux leakage, considering all the radiation particles. The contour plots of mean and standard deviation associated with zero flux leakage are shown in Fig. 20. The results depicted that the conventional composition

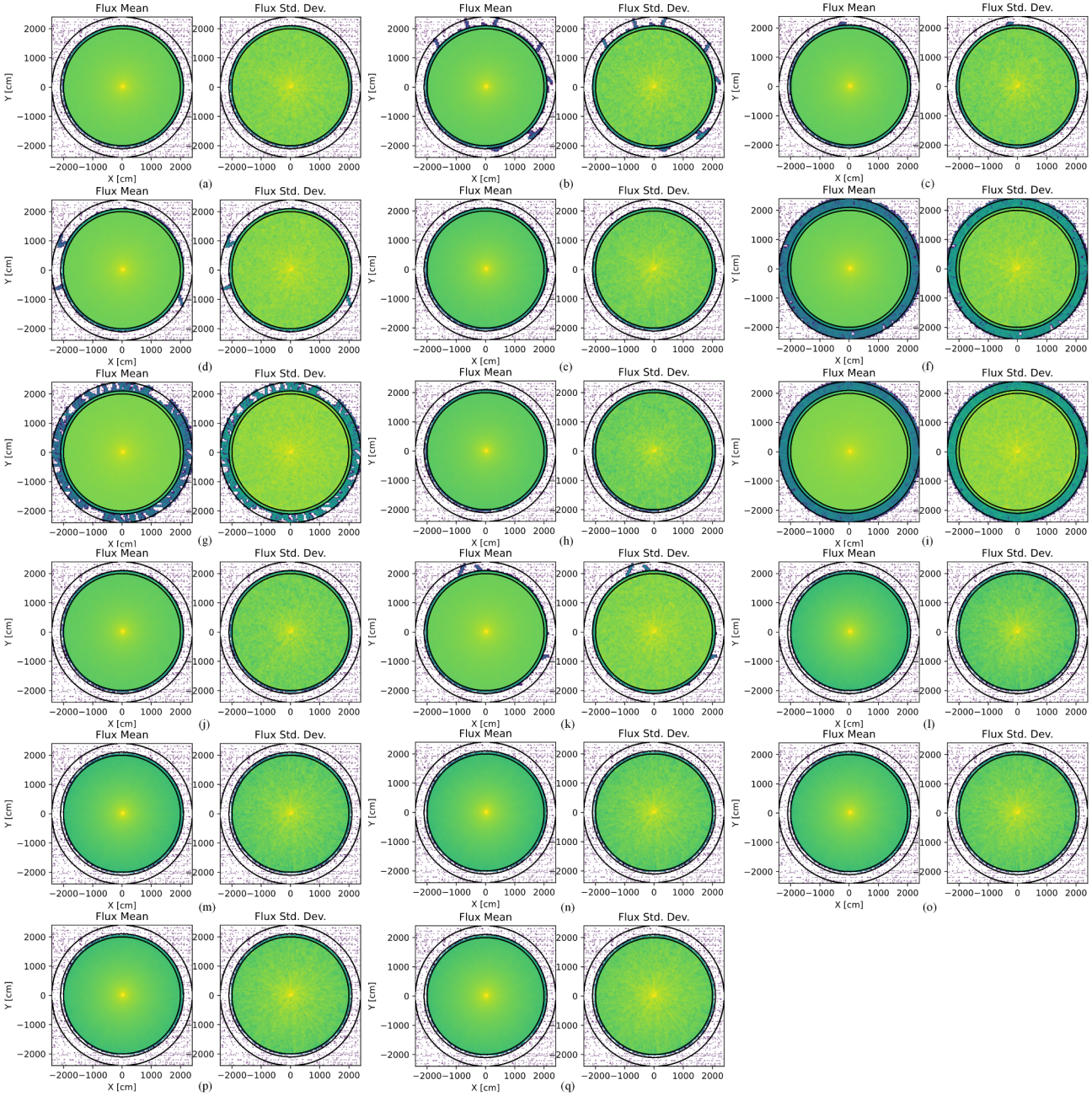


Fig. 15. Flux mean and flux standard deviation of thermal neutron rays interaction with different concrete compositions (**a**) Dez (**b**) Esf (**c**) Gha(**d**) Gun (**e**) Kum (**f**) Luo (**g**) Mad (**h**) Nik (**i**) Say (**j**) Suw (**k**) Zey (**l**) Concrete_1 (**m**) Concrete_2 (**n**) Concrete_3 (**o**) Concrete_4 (**p**) Concrete_5 and (**q**) Concrete_6.

required a section with a minimum thickness of 350 cm, whereas a section developed from concrete_6 composition required a thickness of 150 cm, which is 57.143% less. Further, the TEDR value of conventional concrete composition was calculated as 393.587 pSv/hr, almost ten times more than the TEDR value of concrete_6 composition. The minimum thickness required for other concrete compositions to achieve zero flux leakage can be found in Table S4 in the supplementary section. Assessing the material requirements necessary to attain the desired performance level, the GWP of the proposed composition was calculated to evaluate its environmental impact, comparing it with conventional concrete. The elemental composition of "Concrete_6" serves as a basis for reverse-calculating the necessary materials for its development. A rough estimate of a mix design composition for concrete_6 was made with few assumptions. The additional materials in concrete_6 composition were assumed to be added in their oxide form. This resulted in 136 kg/m^3 WO_3, 1456 kg/m^3 B_2O_3, 365 kg/m^3 Fe_2O_3, and 69 kg/m^3 NiO. Iron content can also be incorporated into the mix design as heavy coarse aggregates, such as hematite or magnetite ores. For cement calculation, it was assumed that cement's calcium and silica content are around 65% and 20%, respectively. This resulted in 432 kg/m^3 cement content. The amorphous

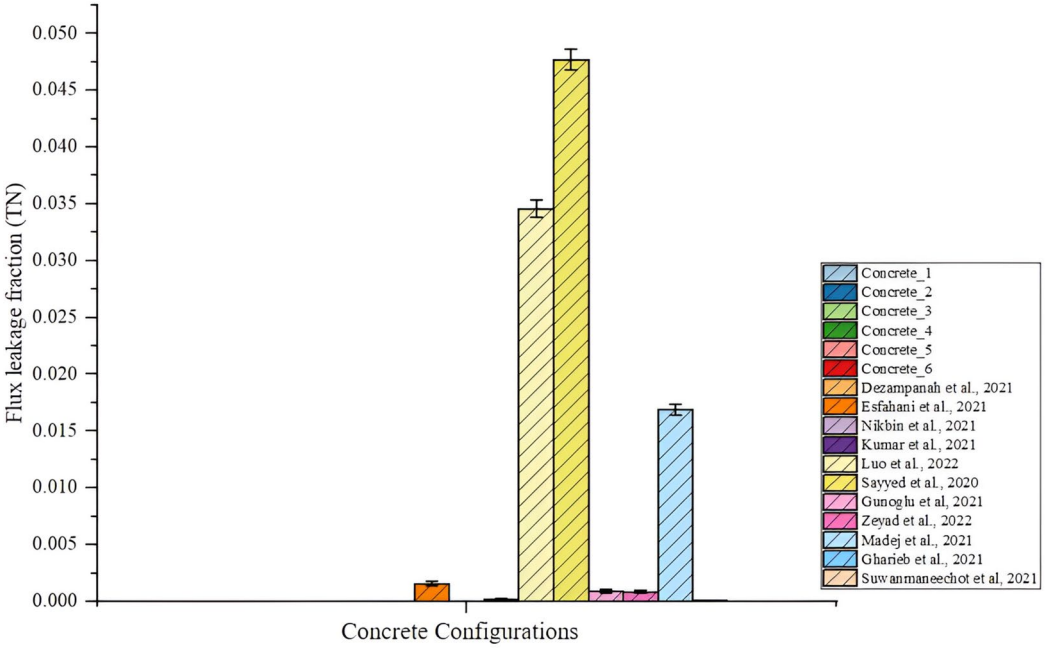


Fig. 16. Mean and standard deviation of thermal neutron flux leakage fraction for different compositions of concrete.

silica was assumed to be contributed by fine sand, which has 75% of the silica content. This resulted in 300 kg/m^3 of fine sand and around 650 kg/m^3 of coarse aggregates. The water content was estimated to be 175 kg/m^3. The particles' gradation and size also matter for better compaction, density, strength, and durability. Based on the considered mix design, the GWP of "Concrete_6" and conventional concrete was computed per cubic meter of concrete.

The calculations revealed that "Concrete_6" emits 163.212 metric tons of equivalent CO_2 per cubic meter, while conventional concrete emits 195.603 metric tons of equivalent CO_2 per cubic meter, which is 19.85% more than concrete_6 composition. Utilizing the concrete volume required for constructing the previously discussed NCS with the required thickness, the overall GWP associated with two different materials was calculated. The calculations revealed that for "Concrete_6," the GWP stands at 1.596×10^5 metric tons of equivalent CO_2, whereas for conventional concrete, it rises to 4.678×10^5 metric tons of equivalent CO_2. Consequently, the employment of "Concrete_6" showcased an impressive 65.89% reduction in GWP compared to conventional concrete while meeting the performance requirements for the targeted NCS. This substantial reduction aligns with the United Nations Sustainable Development Goals (SDGs), particularly SDG 11 (Sustainable Cities and Communities) by promoting environmentally responsible construction materials, SDG 9 (Industry, Innovation, and Infrastructure) by fostering innovative and sustainable material design for advanced NCS, and SDG 7 (Affordable and Clean Energy) by minimizing the carbon footprint of construction of NCS, thus contributing to the global transition towards a low-carbon future.

These findings strongly support the sustainability of the developed concrete configurations, which not only deliver optimal performance but also contribute to a reduced environmental impact. However, a potential concern arises regarding the disposal of concrete containing heavy metals after dismantling the unit, as improper management could lead to soil and groundwater contamination. To address these challenges, future solutions could focus on recycling concretes with heavy metals for the development of low- to moderate-energy radiation-active waste disposal systems, integrating eco-friendly additives, and exploring sustainable recycling or disposal methods for heavy-metal-infused concrete.

Conclusions

The research presented in this paper demonstrates a novel approach to predict optimum overall radiation shielding concrete compositions using combined machine learning and GA. The key findings and conclusions are as follows:

- The linear regression models developed demonstrated strong predictive capability for estimating the effective dose rates from gamma rays, TN, and FN. The high correlation coefficients (0.9055 to 0.9592) and low RMSE values for training and test sets indicate that the models did not suffer from overfitting and can accurately predict the dose rates.
- The optimization of concrete compositions using a multi-objective constrained GA has resulted in the identification of optimal elemental mixes across six different density ranges. These mixes include specific weight

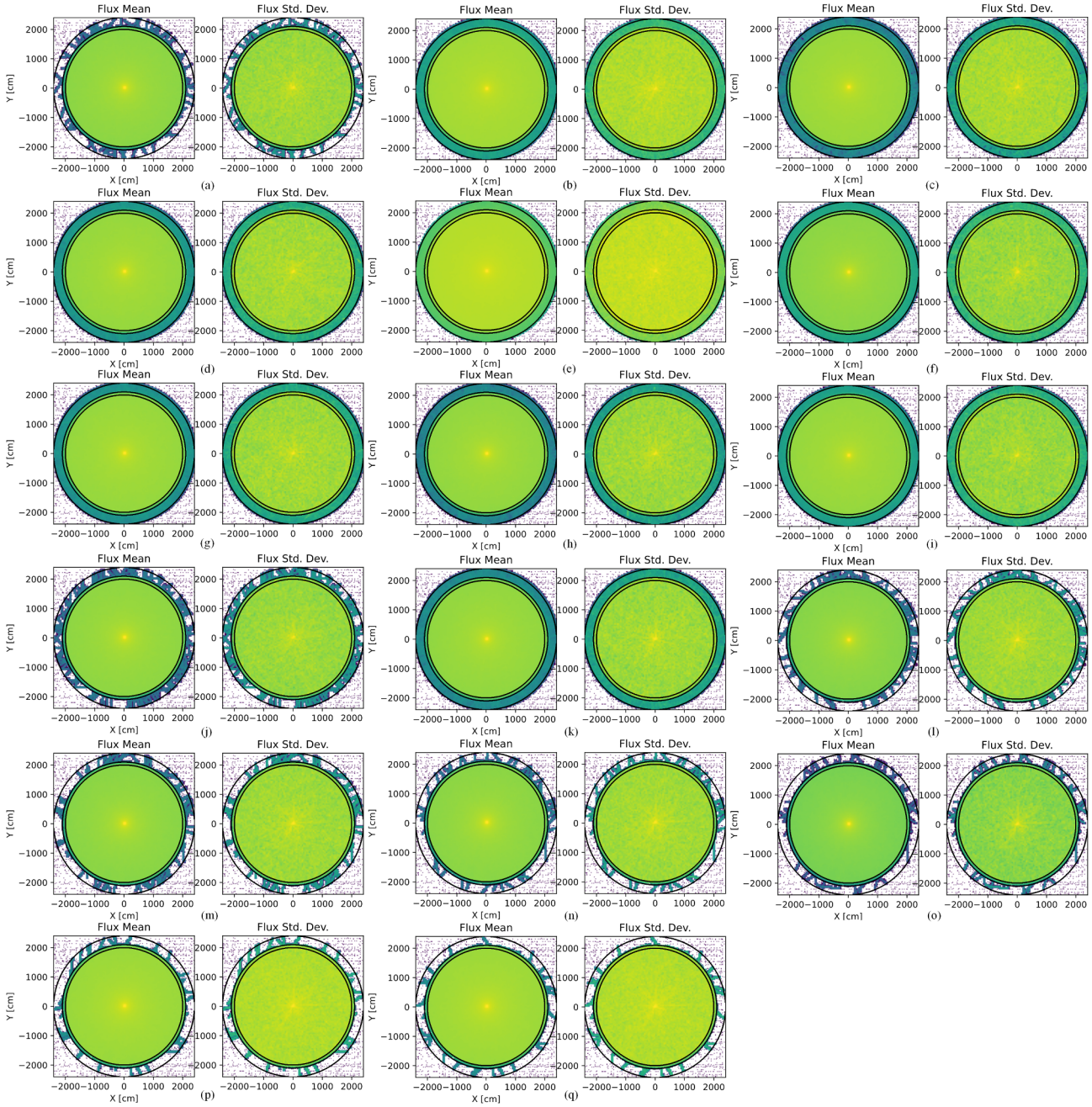


Fig. 17. Flux mean and flux standard deviation of fast neutron rays' interaction with different concrete compositions (**a**) Dez (**b**) Esf (**c**) Gha(**d**) Gun (**e**) Kum (**f**) Luo (**g**) Mad (**h**) Nik (**i**) Say (**j**) Suw (**k**) Zey (**l**) Concrete_1 (**m**) Concrete_2 (**n**) Concrete_3 (**o**) Concrete_4 (**p**) Concrete_5 and (**q**) Concrete_6.

fractions of iron, nickel, tungsten, and boron. Incorporating these elements offers targeted shielding against gamma rays, TN, and FN, ultimately leading to superior overall shielding performance.

- The TEDR for concrete_5 and concrete_6 compositions was 47.331 pSv/hr and 39.908 pSv/hr, respectively, which is 13.12% and 26.74% better than the best existing composition, respectively. Thus, the proposed concrete compositions (concrete_5 and concrete_6) demonstrated the highest overall radiation shielding performance compared to existing compositions in the literature.
- Based on the considered mix design, concrete_6 emits 163.212 metric tons of equivalent CO_2 per cubic meter, while conventional concrete emits 195.603 metric tons per cubic meter, which is 19.85% more. To achieve a zero flux leakage condition, concrete_6 composition required 150 cm thickness, whereas conventional concrete required 350 cm. With consideration of performance level, concrete_6 showcased an impressive approximate 65.89% reduction in GWP compared to conventional concrete for realizing the targeted shielding performance.

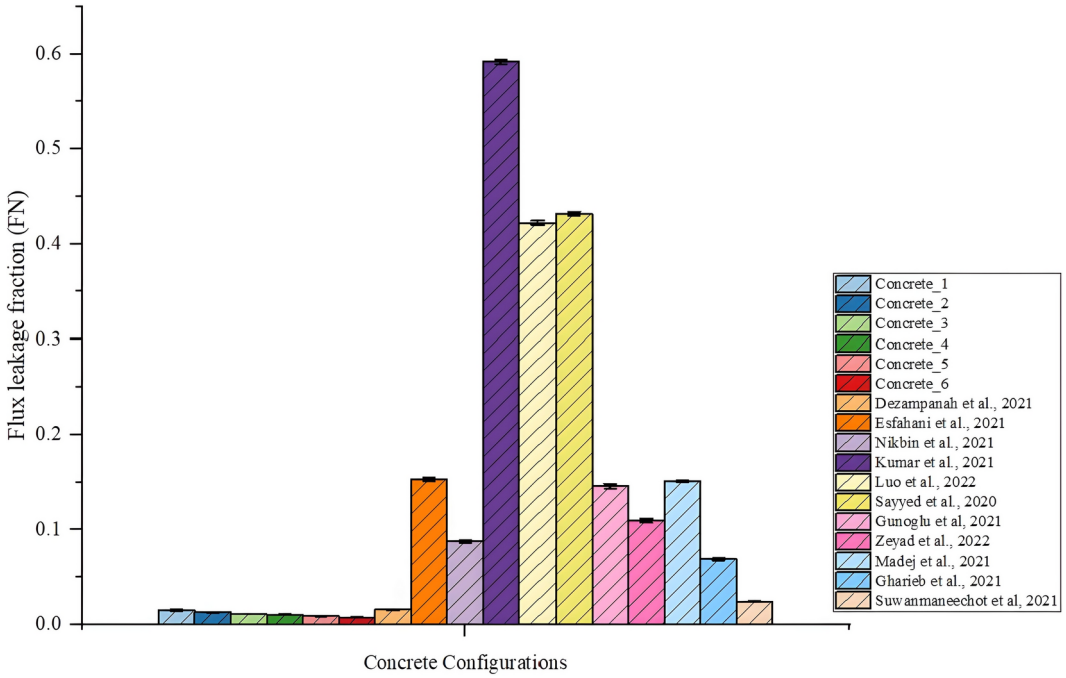


Fig. 18. Mean and standard deviation of fast neutron flux leakage fraction for different compositions of concrete.

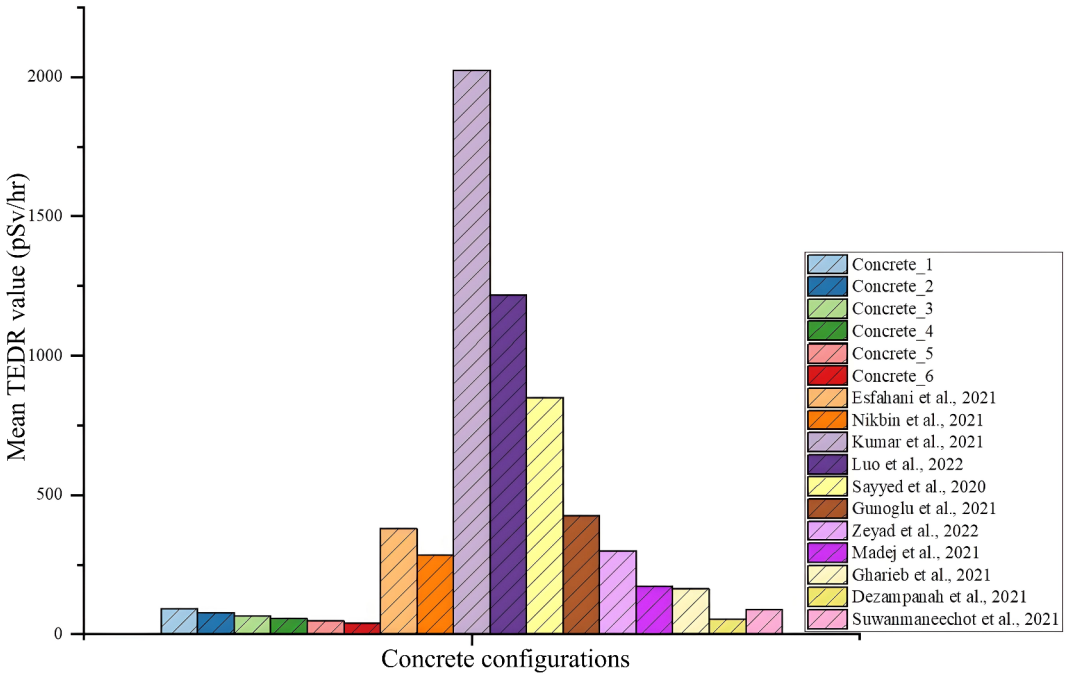


Fig. 19. Overall evaluation of concrete compositions against total radiation based on the total effective flux dosage.

In conclusion, the research has proposed innovative overall radiation-shielding concrete compositions, demonstrating significant advantages in shielding effectiveness, material efficiency, and environmental sustainability. These advancements hold promise for bolstering the resilience of nuclear power plant structures and enhancing various facilities requiring robust overall radiation shielding. Ultimately, these findings stand to propel the evolution of radiation shielding technologies, fostering the design of more efficient and eco-friendly nuclear facilities poised for the challenges of tomorrow.

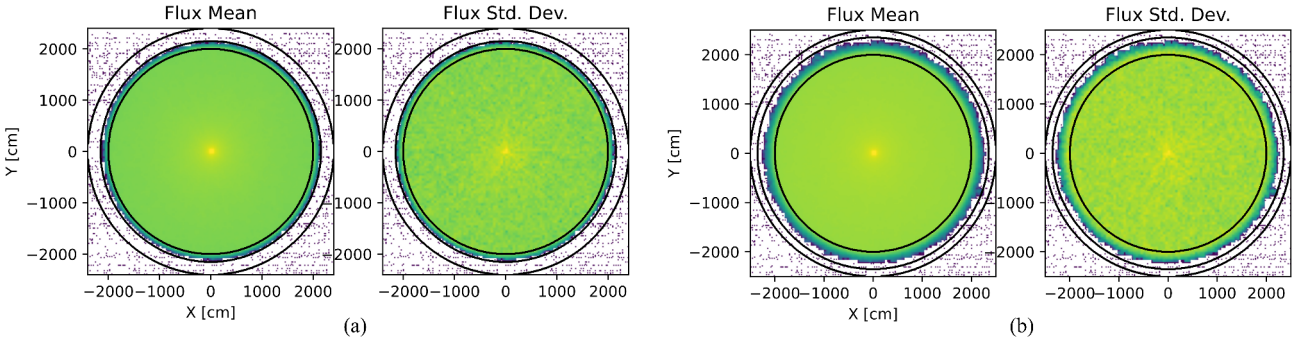


Fig. 20. Nuclear radiation shielding of an NCS made from (**a**) Concrete_6 and (**b**) Conventional Concrete.

Future works

Future research should focus on several key areas to advance the development and application of the proposed concrete compositions for radiation shielding. First, experimental validation is essential to verify their real-world shielding performance. Additionally, selecting the most feasible types and content of raw materials, particularly those closely matching the machine learning outcomes, will be prioritized to facilitate practical implementation. A comprehensive cost–benefit analysis should also be conducted, considering both initial construction costs and long-term factors such as durability, maintenance, and aging effects that may impact shielding efficacy. Additionally, addressing the challenges associated with managing concrete containing toxic elements after the decommissioning of radiation-shielding structures is crucial. Developing safe disposal, recycling, or repurposing protocols will ensure environmental safety and compliance with hazardous waste regulations.

Data availability

Data is provided within the manuscript or supplementary information files.

Received: 8 November 2024; Accepted: 6 February 2025
Published online: 17 February 2025

References

1. Brook, B. W. et al. Why nuclear energy is sustainable and has to be part of the energy mix. *Sustain. Mater. Technol.* **1**, 8–16. https://doi.org/10.1016/j.susmat.2014.11.001 (2014).
2. Parsons, J., Buongiorno, J., Corradini, M. & Petti, D. A fresh look at nuclear energy. *Science* **363**(6423), 105–105. https://doi.org/10.1126/science.aaw5304 (2019).
3. Saenko, V. et al. The Chernobyl accident and its consequences. *Clin. Oncol.* **23**(4), 234–243. https://doi.org/10.1016/j.clon.2011.01.502 (2011).
4. Wang, Q., Chen, X. & Yi-Chong, X. Accident like the Fukushima unlikely in a country with effective nuclear regulation: Literature review and proposed guidelines. *Renew. Sustain. Energy Rev.* **17**, 126–146. https://doi.org/10.1016/j.rser.2012.09.012 (2013).
5. Ishikawa, T. Radiation doses and associated risk from the Fukushima nuclear accident: A review of recent publications. *Asia Pac. J. Pub. Health* **29(2_suppl)**, 18–28. https://doi.org/10.1177/1010539516675 (2017).
6. Marino, F. & Nunziata, L. Long-term consequences of the chernobyl radioactive fallout: An exploration of the aggregate data. *Milbank Q.* **96**(4), 814–857. https://doi.org/10.1111/1468-0009.12358 (2018).
7. Von Wehrden, H. et al. Consequences of nuclear accidents for biodiversity and ecosystem services. *Conserv. Lett.* **5**(2), 81–89. https://doi.org/10.1111/j.1755-263X.2011.00217.x (2012).
8. Kim, J. H. Three principles for radiation safety: Time, distance, and shielding. *Korean J. Pain* **31**(3), 145–146. https://doi.org/10.3344/kjp.2018.31.3.145 (2018).
9. Butler, D. Reactors, residents and risk. *Nature* **472**(7344), 400. https://doi.org/10.1038/472400a (2011).
10. Bamonte, P. & Gambarova, P. G. Properties of concrete required in nuclear power plants. *Infrastruct. Syst. Nucl. energy* https://doi.org/10.1002/9781118536254.ch25 (2014).
11. Ban, C. C. et al. Modern heavyweight concrete shielding: Principles, industrial applications and future challenges; review. *J. Build. Eng.* **39**, 102290. https://doi.org/10.1016/j.jobe.2021.102290 (2021).
12. Mesbahi, A., Alizadeh, G., Seyed-Oskoee, G. & Azarpeyvand, A. A. A new barite–colemanite concrete with lower neutron production in radiation therapy bunkers. *Ann. Nucl. Energy* **51**, 107–111. https://doi.org/10.1016/j.anucene.2012.07.039 (2013).
13. Prabir, B., Pierre, L., & Naus, D. J. Nuclear power plant concrete structures. *Transactions* (2013)
14. Akkurt, I., Basyigit, C., Kilincarslan, S., Mavi, B. & Akkurt, A. Radiation shielding of concretes containing different aggregates. *Cement Concr. Compos.* **28**(2), 153–157. https://doi.org/10.1016/j.cemconcomp.2005.09.006 (2006).
15. Akkurt, I. & Boodaghi Malidarre, R. Monte Carlo simulation study on Barite Concrete for neutron-gamma photon. *Radiat. Eff. Defects Solids* **177**(9–10), 943–956. https://doi.org/10.1080/10420150.2022.2098745 (2022).
16. Awadeen, M., Amin, M., Bakr, R. H. & Tahwia, A. M. Mechanical properties, attenuation coefficient, and microstructure of ultra high-performance heavyweight concrete for radiation shielding applications. *J. Build. Eng.* **82**, 108395. https://doi.org/10.1016/j.jobe.2023.108395 (2024).
17. Choi, Y. S. & Lee, S. M. Fundamental properties and radioactivity shielding performance of concrete recycled cathode ray tube waste glasses and electric arc furnace slag as aggregates. *Progress in Nuclear Energy* **133**, 103649. https://doi.org/10.1016/j.pnucene.2021.103649 (2021).
18. Esen, Y. & Doğan, Z. M. Evaluation of physical and mechanical characteristics of siderite concrete to be used as heavy-weight concrete. *Cem. Concr. Compos.* **82**, 117–127. https://doi.org/10.1016/j.cemconcomp.2017.05.009 (2017).
19. Gharieb, M., Mosleh, Y. A., Alwetaishi, M., Hussein, E. E. & Sultan, M. E. Effect of using heavy aggregates on the high performance concrete used in nuclear facilities. *Constr. Build. Mater.* **310**, 125111. https://doi.org/10.1016/j.conbuildmat.2021.125111 (2021).

20. Gökçe, H. S., Öztürk, B. C., Çam, N. F. & Andiç-Çakır, Ö. Gamma-ray attenuation coefficients and transmission thickness of high consistency heavyweight concrete containing mineral admixture. *Cem. Concr. Compos.* **92**, 56–69. https://doi.org/10.1016/j.cemconcomp.2018.05.015 (2018).
21. Gunoglu, K. & Akkurt, İ. Radiation shielding properties of concrete containing magnetite. *Prog. Nucl. Energy* **137**, 103776. https://doi.org/10.1016/j.pnucene.2021.103776 (2021).
22. Heniegal, A. M., Amin, M., Nagib, S. H., Youssef, H. & Agwa, I. S. Effect of nano ferrosilicon and heavyweight fine aggregates on the properties and radiation shielding of ultra-high performance heavyweight concrete. *Case Stud. Constr. Mater.* **17**, e01543. https://doi.org/10.1016/j.cscm.2022.e01543 (2022).
23. Ibrahim, A. M., Mohamed, A. R., El-Khatib, A. M., Alabsy, M. T. & Elsalamawy, M. Effect of hematite and iron slag as aggregate replacement on thermal, mechanical, and gamma-radiation shielding properties of concrete. *Constr. Build. Mater.* **310**, 125225. https://doi.org/10.1016/j.conbuildmat.2021.125225 (2021).
24. Khan, M. H. et al. Evaluation of mechanical strength, gamma-ray shielding characteristics, and ITZ microstructural properties of heavyweight concrete using nano-silica (SiO2) and barite aggregates. *Constr. Build. Mater.* **419**, 135483. https://doi.org/10.1016/j.conbuildmat.2024.135483 (2024).
25. Khalaf, M. A. et al. Physicomechanical and gamma-ray shielding properties of high-strength heavyweight concrete containing steel furnace slag aggregate. *J. Build. Eng.* **30**, 101306. https://doi.org/10.1016/j.jobe.2020.101306 (2020).
26. Nabil, I. M., El-Samrah, M. G., Omar, A., Tawfic, A. F. & El Sayed, A. F. Experimental, analytical, and simulation studies of modified concrete mix for radiation shielding in a mixed radiation field. *Sci. Rep.* **13**(1), 17637. https://doi.org/10.1038/s41598-023-44978-8 (2023).
27. Sayyed, M. I. et al. Application of the MCNP 5 code to simulate the shielding features of concrete samples with different aggregates. *Radiat. Phys. Chem.* **174**, 108925. https://doi.org/10.1016/j.radphyschem.2020.108925 (2020).
28. Thomas, C. et al. Effect of elevated temperature on the mechanical properties and microstructure of heavy-weight magnetite concrete with steel fibers. *Cem. Concr. Compos.* **103**, 80–88. https://doi.org/10.1016/j.cemconcomp.2019.04.029 (2019).
29. Wang, Q. et al. Influence of polypropylene fibers on the mechanical properties of radiation shielding concrete with barite aggregates. *J. Build. Eng.* **79**, 107820. https://doi.org/10.1016/j.jobe.2023.107820 (2023).
30. Xia, Y. et al. Effects of colemanite, heavy aggregates and lead fibers on physical mechanics and radiation shielding properties of high-performance radiation shielding concrete. *J. Build. Eng.* **96**, 110496. https://doi.org/10.1016/j.jobe.2024.110496 (2024).
31. Xia, Y. et al. Iron-rich industrial waste enhanced low-carbon radiation shielding functional composites. *J. Clean. Prod.* **449**, 141649. https://doi.org/10.1016/j.jclepro.2024.141649 (2024).
32. Zayed, A. M. et al. Influence of heavyweight aggregates on the physico-mechanical and radiation attenuation properties of serpentine-based concrete. *Constr. Build. Mater.* **260**, 120473. https://doi.org/10.1016/j.conbuildmat.2020.120473 (2020).
33. Zeyad, A. M., Hakeem, I. Y., Amin, M., Tayeh, B. A. & Agwa, I. S. Effect of aggregate and fibre types on ultra-high-performance concrete designed for radiation shielding. *J. Build. Eng.* **58**, 104960. https://doi.org/10.1016/j.jobe.2022.104960 (2022).
34. Zhou, Y. et al. Research on the shielding performance of concrete in a 60Co irradiation environment. *Nucl. Eng. Des.* **413**, 112575. https://doi.org/10.1016/j.nucengdes.2023.112575 (2023).
35. Ali, M. A., Tawfic, A. F., Abdelgawad, M. A., Wagih, M. & Omar, A. Potential uses of different sustainable concrete mixtures in gamma and neutrons shielding purposes. *Prog. Nucl. Energy* **157**, 104598. https://doi.org/10.1016/j.pnucene.2023.104598 (2023).
36. Eid, M. S. et al. Implementation of waste silicate glass into composition of ordinary cement for radiation shielding applications. *Nucl. Eng. Technol.* **54**(4), 1456–1463. https://doi.org/10.1016/j.net.2021.10.007 (2022).
37. Esfahani, S. M. R. A. et al. Mechanical and gamma-ray shielding properties and environmental benefits of concrete incorporating GGBFS and copper slag. *J. Build. Eng.* **33**, 101615. https://doi.org/10.1016/j.jobe.2020.101615 (2021).
38. Gashti, M. F., Mousavinejad, S. H. G. & Khaleghi, S. J. Evaluation of gamma and neutron radiation shielding properties of the GGBFS based geopolymer concrete. *Constr. Build. Mater.* **367**, 130308. https://doi.org/10.1016/j.conbuildmat.2023.130308 (2023).
39. Kumar, S., Mann, K. S., Singh, T. & Singh, S. Investigations on the gamma-ray shielding performance of green concrete using theoretical, experimental and simulation techniques. *Prog. Nucl. Energy* **134**, 103654. https://doi.org/10.1016/j.pnucene.2021.103654 (2021).
40. Luo, L. et al. Effects of high temperatures on the splitting tensile strength and gamma ray shielding performance of radiation shielding concrete. *Constr. Build. Mater.* **343**, 127953. https://doi.org/10.1016/j.conbuildmat.2022.127953 (2022).
41. Moradllo, M. K. et al. Use of borosilicate glass powder in cementitious materials: Pozzolanic reactivity and neutron shielding properties. *Cem. Concr. Compos.* **112**, 103640. https://doi.org/10.1016/j.cemconcomp.2020.103640 (2020).
42. Park, J., Her, S., Cho, S., Woo, S. M. & Bae, S. Synthesis and characterization of Polyethylene/B4C composite, and its neutron shielding performance in cementitious materials: Experimental and simulation studies. *Cem. Concr. Compos.* **129**, 104458. https://doi.org/10.1016/j.cemconcomp.2022.104458 (2022).
43. Piotrowski, T. Neutron shielding evaluation of concretes and mortars: A review. *Constr. Build. Mater.* **277**, 122238. https://doi.org/10.1016/j.conbuildmat.2020.122238 (2021).
44. Singh, S. & Singh, K. On the use of green concrete composite as a nuclear radiation shielding material. *Prog. Nucl. Energy* **136**, 103730. https://doi.org/10.1016/j.pnucene.2021.103730 (2021).
45. Madej, D., Silarski, M. & Parzych, S. Design, structure, microstructure and gamma radiation shielding properties of refractory concrete materials containing Ba-and Sr-doped cements. *Mater. Chem. Phys.* **260**, 124095. https://doi.org/10.1016/j.matchemphys.2020.124095 (2021).
46. Bashter, I. I. Calculation of radiation attenuation coefficients for shielding concretes. *Ann. Nucl. Energy* **24**(17), 1389–1401. https://doi.org/10.1016/S0306-4549(97)00003-0 (1997).
47. Yan, J. et al. Study on mechanical behavior of containment in nuclear power plant during prestressing construction. *Nucl. Eng. Des.* **338**, 247–260. https://doi.org/10.1016/j.nucengdes.2018.08.022 (2018).
48. Zalegowski, K., Piotrowski, T., Garbacz, A. & Adamczewski, G. Relation between microstructure, technical properties and neutron radiation shielding efficiency of concrete. *Constr. Build. Mater.* **235**, 117389. https://doi.org/10.1016/j.conbuildmat.2019.117389 (2020).
49. Ali, M. A., Tawfic, A. F., Abdelgawad, M. A., Mahdy, M. & Omar, A. Gamma and neutrons shielding using innovative fiber reinforced concrete. *Prog. Nucl. Energy* **145**, 104133. https://doi.org/10.1016/j.pnucene.2022.104133 (2022).
50. Al-Saleh, W. M., Elsafi, M., Almutairi, H. M., Nabil, I. M. & El-Nahal, M. A. A comprehensive study of the shielding ability from ionizing radiation of different mortars using iron filings and bismuth oxide. *Sci. Rep.* **14**(1), 10014. https://doi.org/10.1038/s41598-024-60188-2 (2024).
51. Bevelacqua, J. J. & Mortazavi, S. M. J. Neutron shielding concrete in medical applications. In *Micro and Nanostructured Composite Materials for Neutron Shielding Applications* 219–237 (Woodhead Publishing, 2020). https://doi.org/10.1016/B978-0-12-819459-1.00008-8.
52. Dezhampanah, S., Nikbin, I. M., Mehdipour, S., Mohebbi, R. & Moghadam, H. Fiber-reinforced concrete containing nano-TiO2 as a new gamma-ray radiation shielding materials. *J. Build. Eng.* **44**, 102542. https://doi.org/10.1016/j.jobe.2021.102542 (2021).
53. El-Nahal, M. A. et al. Understanding the effect of introducing micro- and nanoparticle bismuth oxide (Bi2O3) on the gamma ray shielding performance of novel concrete. *Materials* **14**(21), 6487. https://doi.org/10.3390/ma14216487 (2021).
54. Elsadany, R. A., Elsadany, R. A., Al-Tersawy, S. H., Metwaly, K. A. & Elgammal, W. A. Evaluation of gamma ray attenuation properties of normal concrete with some nano materials using Monte Carlo simulation and experimental measurements. *Arab J. Nucl. Sci. Appl.* **56**(3), 129–144. https://doi.org/10.21608/ajnsa.2023.173903.1678 (2023).

55. Fathy, I. N. et al. Enhancing mechanical and radiation shielding properties of concrete with lead monoxide and granodiorite: Individual and synergistic effects at micro and nano particle scales. *Struct. Concr.* https://doi.org/10.1002/suco.202400454 (2024).
56. Khalaf, M. A., Cheah, C. B., Ramli, M., Ahmed, N. M. & Al-Shwaiter, A. Effect of nano zinc oxide and silica on mechanical, fluid transport and radiation attenuation properties of steel furnace slag heavyweight concrete. *Constr. Build. Mater.* **274**, 121785. https://doi.org/10.1016/j.conbuildmat.2020.121785 (2021).
57. Khemngern, S., Wongsawaeng, D., Jongvivatsakul, P. & Nuaklong, P. Mechanical and thermal neutron attenuation properties of concrete reinforced with low-dose gamma irradiated PETE fibers and sodium borate. *Eng. J.* **24**(3), 1–10. https://doi.org/10.4186/ej.2020.24.3.1 (2020).
58. Martellucci, R. & Torsello, D. Potential of biochar reinforced concrete as neutron shielding material. *Nucl. Eng. Technol.* **54**(9), 3448–3451. https://doi.org/10.1016/j.net.2022.03.031 (2022).
59. Masoud, M. A. et al. Valorization of hazardous chrysotile by H3BO3 incorporation to produce an innovative eco-friendly radiation shielding concrete: Implications on physico-mechanical, hydration, microstructural, and shielding properties. *Cem. Concr. Compos.* **141**, 105120. https://doi.org/10.1016/j.cemconcomp.2023.105120 (2023).
60. Nikbin, I. M. et al. Effect of high temperature on mechanical and gamma ray shielding properties of concrete containing nano-TiO2. *Radiat. Phys. Chem.* **174**, 108967. https://doi.org/10.1016/j.radphyschem.2020.108967 (2020).
61. Paul, M. B., Ankan, A. D., Deb, H. & Ahasan, M. M. A Monte Carlo simulation model to determine the effective concrete materials for fast neutron shielding. *Radiat. Phys. Chem.* **202**, 110476. https://doi.org/10.1016/j.radphyschem.2022.110476 (2023).
62. Şensoy, A. T. & Gökçe, H. S. Simulation and optimization of gamma-ray linear attenuation coefficients of barite concrete shields. *Constr. Build. Mater.* **253**, 119218. https://doi.org/10.1016/j.conbuildmat.2020.119218 (2020).
63. Soni, B. K. et al. Novel concrete compositions for γ-rays and neutron shielding using WC and B4C. *Results Mater.* **10**, 100177. https://doi.org/10.1016/j.rinma.2021.100177 (2021).
64. Suwanmaneechot, P., Bongkarn, T., Joyklad, P. & Julphunthong, P. Experimental and numerical evaluation of gamma-ray attenuation characteristics of concrete containing high-density materials. *Constr. Build. Mater.* **294**, 123614. https://doi.org/10.1016/j.conbuildmat.2021.123614 (2021).
65. Tasnim, A., Sahadath, M. H. & Khan, M. N. I. Development of high-density radiation shielding materials containing BaSO4 and investigation of the gamma-ray attenuation properties. *Radiat. Phys. Chem.* **189**, 109772. https://doi.org/10.1016/j.radphyschem.2021.109772 (2021).
66. Tohver, H. et al. Assessing shielding material performance: Benchmarking of Monte Carlo codes for oil shale and basalt-boron fiber concretes. *Nucl. Eng. Des.* **417**, 112811. https://doi.org/10.1016/j.nucengdes.2023.112811 (2024).
67. Zayed, A. M. et al. From discarded waste to valuable products: Barite combination with chrysotile mine waste to produce radiation-shielding concrete. *Constr. Build. Mater.* **417**, 135334. https://doi.org/10.1016/j.conbuildmat.2024.135334 (2024).
68. Zayed, A. M. et al. Physical, mechanical, and radiation attenuation properties of serpentine concrete containing boric acid. *Constr. Build. Mater.* **272**, 121641. https://doi.org/10.1016/j.conbuildmat.2020.121641 (2021).
69. Mahmoud, A. A. et al. Influence of sustainable waste granite, marble and nano-alumina additives on ordinary concretes: A physical, structural, and radiological study. *Scientific Reports* **14**(1), 22011. https://doi.org/10.1038/s41598-024-72222-4 (2024).
70. Onaizi, A. M. et al. Radiation-shielding concrete: A review of materials, performance, and the impact of radiation on concrete properties. *J. Build. Eng.* https://doi.org/10.1016/j.jobe.2024.110800 (2024).
71. Shi, D. et al. Valorization of steel slag into sustainable high-performance radiation shielding concrete. *J. Build. Eng.* **91**, 109650. https://doi.org/10.1016/j.jobe.2024.109650 (2024).
72. Tyagi, G., Singhal, A., Routroy, S., Bhunia, D. & Lahoti, M. Radiation Shielding Concrete with alternate constituents: An approach to address multiple hazards. *J. Hazard. Mater.* **404**, 124201. https://doi.org/10.1016/j.jhazmat.2020.124201 (2021).
73. Xia, Y. et al. Value-added recycling of cathode ray tube funnel glass into high-performance radiation shielding concrete. *Resour. Conserv. Recycl.* **199**, 107252. https://doi.org/10.1016/j.resconrec.2023.107252 (2023).
74. Schunck, N. & Regnier, D. Theory of nuclear fission. *Prog. Part. Nucl. Phys.* **125**, 103963. https://doi.org/10.1016/j.ppnp.2022.103963 (2022).
75. Amirabadi, E. A., Salimi, M., Ghal-Eh, N., Etaati, G. R. & Asadi, H. Study of neutron and gamma radiation protective shield. *Int. J. Innov. Appl. Stud.* **3**(4), 1079–1085 (2013).
76. Aygün, B. Neutron and gamma radiation shielding Ni based new type super alloys development and production by Monte Carlo Simulation technique. *Radiat. Phys. Chem.* **188**, 109630. https://doi.org/10.1016/j.radphyschem.2021.109630 (2021).
77. Cunningham, J. R., & Dance, D. R. Interactions of Radiation with Matter (Chapter 2). *International Atomic Energy Agency (IAEA)* (2014)
78. Romano, P. K. et al. OpenMC: A state-of-the-art Monte Carlo code for research and development. *Ann. Nucl. Energy* **82**, 90–97. https://doi.org/10.1016/j.anucene.2014.07.048 (2015).
79. Swinehart, D. F. The beer-lambert law. *J. Chem. Educ.* **39**(7), 333 (1962).
80. Hughes, D. J. & Schwartz, R. B. *Neutron cross sections* Vol. 325 (Brookhaven National Laboratory, 1958).
81. Fisher, D. R. & Fahey, F. H. Appropriate use of effective dose in radiation protection and risk assessment. *Health phys.* **113**(2), 102–109. https://doi.org/10.1097/HP.0000000000000674 (2017).
82. Battistoni, G. et al. Overview of the FLUKA code. *Ann. Nucl. Energy* **82**, 10–18. https://doi.org/10.1016/j.anucene.2014.11.007 (2015).
83. Agostinelli, S. et al. GEANT4—a simulation toolkit. *Nucl. Instrum. Methods Phys. Res., Sect. A* **506**(3), 250–303. https://doi.org/10.1016/S0168-9002(03)01368-8 (2003).
84. Thoennessen, M. & Thoennessen, M. Neutron-Induced Reactions. *Discov. Iso. : Complet. Compil.* https://doi.org/10.1007/978-3-319-31763-2_7 (2016).
85. Nakashima, Y., Minato, S., Kawano, M., Tsujimoto, T. & Katsurayama, K. Gamma-ray energy spectra observed around a nuclear reactor. *J. Radiat. Res.* **12**(3–4), 138–147. https://doi.org/10.1269/jrr.12.138 (1971).
86. Makii, H. et al. Effects of the nuclear structure of fission fragments on the high-energy prompt fission γ-ray spectrum in U 235 (n th, f). *Phys. Rev. C* **100**(4), 044610. https://doi.org/10.1103/PhysRevC.100.044610 (2019).
87. Shimazu, Y. Reactor physics of MSR. In *Molten Salt Reactors and Thorium Energy* 93–109 (Woodhead Publishing, 2017). https://doi.org/10.1016/B978-0-08-101126-3.00004-X.
88. Petoussi-Henss, N. et al. Conversion coefficients for radiological protection quantities for external radiation exposures. *Ann. ICRP* **40**(2–5), 1–257. https://doi.org/10.1016/j.radphyschem.2022.110476 (2010).
89. Verbeke, J. M., Hagmann, C. & Wright, D. Simulation of neutron and gamma ray emission from fission and photofission. *Lawrence Livermore Nat. Lab., Livermore CA, UCRL-AR-228518* **4**, 40 (2010).
90. Elamary, A. S. & Taha, I. B. Determining the shear capacity of steel beams with corrugated webs by using optimised regression learner techniques. *Materials* **14**(9), 2364. https://doi.org/10.3390/ma14092364 (2021).
91. Pfeifer, P. E. Testing Model Significance Using the F-Test.
92. Stunt, J. et al. Why we habitually engage in null-hypothesis significance testing: A qualitative study. *Plos one* **16**(10), e0258330. https://doi.org/10.1371/journal.pone.0258330 (2021).
93. Sivanandam, S. N., Deepa, S. N., Sivanandam, S. N. & Deepa, S. N. *Genetic algorithms* 15–37 (Springer Berlin Heidelberg, 2008). https://doi.org/10.1007/978-3-540-73190-0_2.
94. Diehl, R. Gamma-ray production and absorption processes. In *The Universe in Gamma Rays* 9–25 (Springer Berlin Heidelberg, 2001).

95. Jin, S. & Gong, J. A simplified method for probabilistic seismic risk evaluation of nuclear containment structure. *Int. J. Press. Vessel. Pip.* **189**, 104283. https://doi.org/10.1016/j.ijpvp.2020.104283 (2021).
96. Kurad, R., Silvestre, J. D., de Brito, J. & Ahmed, H. Effect of incorporation of high volume of recycled concrete aggregates and fly ash on the strength and global warming potential of concrete. *J. Clean. Prod.* **166**, 485–502. https://doi.org/10.1016/j.jclepro.2017.07.236 (2017).
97. Nuss, P. & Eckelman, M. J. Life cycle assessment of metals: A scientific synthesis. *PloS one* **9**(7), e101298. https://doi.org/10.1371/journal.pone.0101298 (2014).

Acknowledgements
The authors would like to express sincere gratitude to Dr. Kaling Taki, Assistant Professor at the Indian Institute of Technology Guwahati, for his invaluable guidance, insights, and support throughout this research. His expertise and mentorship have been instrumental in shaping this work, and his encouragement has been a source of motivation. Further, the authors would also like to thank the Prime Minister's Research Fellowship (PMRF) for funding the PhD of Sanchit Saxena and the PMRF review committee for their invaluable suggestions.

Author contributions
S.S. conceptualized the manuscript, prepared the methodology, developed the codes, performed formal analysis, prepared the figures, and wrote the original draft. H.S. supervised the work, and reviewed and edited the manuscript.

Declarations

Competing interests
The authors declare no competing interests.

Additional information
Supplementary Information The online version contains supplementary material available at https://doi.org/10.1038/s41598-025-89683-w.

Correspondence and requests for materials should be addressed to H.S.

Reprints and permissions information is available at www.nature.com/reprints.

Publisher's note Springer Nature remains neutral with regard to jurisdictional claims in published maps and institutional affiliations.

Open Access This article is licensed under a Creative Commons Attribution-NonCommercial-NoDerivatives 4.0 International License, which permits any non-commercial use, sharing, distribution and reproduction in any medium or format, as long as you give appropriate credit to the original author(s) and the source, provide a link to the Creative Commons licence, and indicate if you modified the licensed material. You do not have permission under this licence to share adapted material derived from this article or parts of it. The images or other third party material in this article are included in the article's Creative Commons licence, unless indicated otherwise in a credit line to the material. If material is not included in the article's Creative Commons licence and your intended use is not permitted by statutory regulation or exceeds the permitted use, you will need to obtain permission directly from the copyright holder. To view a copy of this licence, visit http://creativecommons.org/licenses/by-nc-nd/4.0/.

© The Author(s) 2025

Reproduced with permission of copyright owner. Further reproduction prohibited without permission.